arXiv:1602.04312v1 [math.NA] 13 Feb 2016

The Linearized Inverse Problem in Multifrequency Electrical Impedance Tomography

Giovanni S. Alberti* Habib Ammari* Bangti Jin† Jin-Keun Seo‡
Wenlong Zhang§

June 9, 2022

Abstract

This paper provides a mathematical analysis of the linearized inverse problem in multifrequency electrical impedance tomography. We consider the isotropic conductivity distribution with a finite number of unknown inclusions with different frequency dependence, as is often seen in biological tissues. We discuss reconstruction methods for both fully known and partially known spectral profiles, and demonstrate in the latter case the successful employment of difference imaging. We also study the reconstruction with an imperfectly known boundary, and show that the multifrequency approach can eliminate modeling errors and can recover almost all inclusions. In addition, we develop an efficient group sparse recovery algorithm for the robust solution of related linear inverse problems. Several numerical simulations are presented to illustrate and validate the approach.

Keywords: multifrequency electrical impedance tomography, linearized inverse problem, reconstruction, imperfectly known boundary, group sparsity, regularization.

MSC (2010): 35R30, 49N45, 65N21, 92C55, 65F22.

1 Introduction

Electrical impedance tomography (EIT) is a diffusive imaging modality that recovers the conductivity distribution of an electrically conducting object by using electrodes to measure the resulting voltage on its boundary, induced by multiple known injected currents. It is safe, cheap and portable, and is potentially applicable to clinical imaging in a range of areas [27]. However, the EIT inverse problem is severely ill-posed, and has thus shown only modest image quality when compared with other modalities [12]. This has motivated numerous mathematical studies on EIT imaging techniques including small anomaly conductivity imaging [8, 9, 11, 38] and hybrid conductivity imaging [3, 4, 5, 7, 10, 18, 42, 47, 53].

Static imaging, which aims to recover absolute conductivity values, has so far achieved only limited success in practice. This is attributed to the fact that the electrode voltages are insensitive to localized conductivity changes, but very sensitive to forward modelling errors (e.g., the boundary shape, the electrode positions, and the contact impedances). Therefore, apart from accurate data, a very accurate forward model is required for the success of static imaging; however, this is commonly difficult to obtain

*Department of Mathematics, ETH Zürich, Räamistrasse 101, 8092 Zürich, Switzerland. (Email: giovanni.alberti@sam.math.ethz.ch, habib.ammari@math.ethz.ch)

†Department of Computer Science, University College London, Gower Street, London WC1E 6BT, UK. (Email: b.jin@ucl.ac.uk)

‡Department of Computational Science and Engineering, Yonsei University, 50 Yonsei-Ro, Seodaemun-Gu, Seoul 120-749, Korea. (Email: seoj@yonsei.ac.kr)

§Department of Mathematics and Applications, École Normale Supérieure, 45 Rue d'Ulm, 75005 Paris, France. (Email: wenlong.zhang@ens.fr)

in practice. A prominent idea is to use difference imaging, in the hope of canceling out errors due to boundary shape, the electrode positions, and other systematic errors. A traditional approach to these issues is the time difference imaging, which produces an image of the resulting conductivity change by inverting a linearized sensitivity model. A second approach is multifrequency electrical impedance tomography (mfEIT), also known as EIT spectroscopy, which has also attracted attention in recent years.

Imaging by mfEIT exploits the frequency dependence of the conductivity distribution. Experimental research has found that the conductivity of many biological tissues varies strongly with respect to the frequency within certain frequency ranges [19, 17, 39]. In [6], the authors analytically exhibit the fundamental mechanisms underlying the fact that effective biological tissue electrical properties and their frequency dependence reflect the tissue composition and physiology. For doing so, a homogenization theory is derived to describe the effective admittivity of cell suspensions. In mfEIT, the boundary voltage measurements are recorded simultaneously, while varying the modulation frequency of the injected current. The multifrequency approach is expected to be especially useful for the diagnostic imaging of conditions such as acute stroke, brain injury, and breast cancer, because patients are admitted into care after the onset of the pathology and thus lack a baseline record for healthy tissue. In these cases, time difference imaging may not be used.

There have been several studies on frequency-difference imaging [23, 44, 54]. For example, a multifrequency EIT experimental design which provides up to 64 electrodes for imaging the head was described in [54]. In these works, the simple frequency difference (between two neighboring frequencies) was often employed. Seo et al. [46] proposed a weighted frequency difference imaging technique, which is based on a suitable weighted voltage difference between any *two* sets of data. It was numerically shown that the approach can accommodate geometrical errors, including imperfectly known boundary. This approach can improve the reconstruction quality when the background is frequency dependent. Recently, Malone et al. [40] proposed a nonlinear reconstruction scheme, which uses all multifrequency data directly to reconstruct the volume fraction distribution of the tissues, and validated the approach on phantom experimental data; see also [41] for a recent probabilistic reconstruction-classification based technique. We also refer to [35] for a related mathematical study.

This work analyzes mfEIT in the linearized regime, by linearizing the forward model around the homogeneous background conductivity, as customarily adopted in practice [27, 1]. We shall discuss both the mathematically convenient continuum model and the practically popular complete electrode model. Our main contributions are as follows. First, we discuss mfEIT reconstruction for spectral profiles that are known, or partially known, or unknown, and also generalize the existing studies, especially [46]. Second, we rigorously justify mfEIT for handling geometrical errors. Third, we present a novel group sparse reconstruction algorithm of iterative shrinkage type, which is easily implemented and converges quickly. Extensive numerical experiments confirm our discussions.

The rest of the paper is organized as follows. In Section 2, we mathematically formulate mfEIT using a continuum model, and analyze three important scenarios, depending on the knowledge of the spectral profiles. Then, in Section 3, we illustrate the potential of mfEIT in handling the modelling error due to an imperfectly known boundary shape. These analyses are then extended to the more realistic complete electrode model in Section 4. In Section 5, we present a novel group sparse reconstruction algorithm. Last, in Section 6, extensive numerical experiments are presented to illustrate the approach both with a known and with an imperfectly known boundary.

2 The Continuum Model

In this section, we mathematically formulate mfEIT in the continuum model with a perfectly known boundary. The extensions to the case of an imperfectly known boundary and to the complete electrode model will be discussed in Sections 3 and 4 below. Let Ω be an open bounded domain in $\mathbb{R}^d$ $(d = 2, 3)$, occupied by the object under investigation, with its smooth boundary $\partial\Omega$. The mfEIT forward problem reads: for any given input current $f \in L^2_\diamond(\partial\Omega) := \{g \in L^2(\Omega) : \int_{\partial\Omega} g\, ds = 0\}$ and the frequency-dependent

conductivity distribution $\sigma(x,\omega)$, find $u(\cdot,\omega) \in H^1(\Omega)$ such that

$$\begin{cases} -\nabla \cdot (\sigma(x,\omega)\nabla u(x,\omega)) = 0 \quad \text{in } \Omega, \\ \sigma(x,\omega)\dfrac{\partial u}{\partial \nu} = f(x) \quad \text{on } \partial\Omega, \\ \displaystyle\int_{\partial\Omega} u(x,\omega)\, ds = 0, \end{cases} \tag{2.1}$$

where ω denotes the frequency and ν is the unit outward normal vector to the boundary $\partial\Omega$. The weak formulation of problem (2.1) is to find $u = u(\cdot,\omega) \in H_\diamond(\Omega) := \{v \in H^1(\Omega) : \int_{\partial\Omega} v ds = 0\}$ such that

$$\int_\Omega \sigma \nabla u \cdot \nabla v\, dx = \int_{\partial\Omega} f v\, ds, \qquad v \in H^1(\Omega).$$

Throughout this paper, we assume that the frequency-dependent conductivity distribution $\sigma(x,\omega)$ takes the separable form

$$\sigma(x,\omega) = \sum_{k=0}^{K} \sigma_k(x) s_k(\omega), \tag{2.2}$$

where $K+1$ is the number of spectral profiles, $\{s_k(\omega)\}_{k=0}^K$ are a collection of (possibly only partially known) material spectra, often referred to as endmembers, and $\{\delta\sigma_k(x)\}_{k=0}^K$ are scalar functions representing the corresponding proportions, also known as abundances, following the terminology in the hyperspectral unmixing literature [34]. Further, we shall assume

$$\begin{aligned} \sigma_0(x) &= 1 + \delta\sigma_0(x), \\ \sigma_k(x) &= \delta\sigma_k(x), \quad k = 1, \dots, K, \end{aligned}$$

where the $\delta\sigma_k$s are small (in suitable $L^p(\Omega)$ norms) so that a linearized model is valid. The $\delta\sigma_k$s, including the background $\delta\sigma_0$, are all unknown and represent the small inclusions/anomalies in the object Ω. We assume that they have compact spatial supports in the domain Ω, and are disjoint from each other. We also assume that the background spectral profile $s_0(\omega)$ is known.

In order to probe the conductivity distribution $\sigma(x,\omega)$ within the object, we apply N linearly independent input currents $\{f_n\}_{n=1}^N \subset L^2_\diamond(\partial\Omega)$ to the boundary $\partial\Omega$. Let $\{u_n \equiv u_n(x,\omega)\}_{n=1}^N \subset H^1_\diamond(\Omega)$ be the corresponding solutions to (2.1), i.e.,

$$\int_\Omega \sigma \nabla u_n \cdot \nabla v\, dx = \int_{\partial\Omega} f_n v\, ds, \qquad v \in H^1(\Omega). \tag{2.3}$$

Then the mfEIT inverse problem is to recover the abundances $\{\delta\sigma_k\}_{k=0}^K$ and/or other quantities of interest from measurements of the electrode voltages $\{u_n(x,\omega)\}_{n=1}^N$ on the boundary $\partial\Omega$ at a number of modulating frequencies $\{\omega_q\}_{q=1}^Q$.

Next we derive the linearized model for the inverse problem, which is customarily employed in EIT applications due to its computational convenience [27, 1]. In this work, we adopt a linearized model based on an integral representation. Let $v_m \in H^1_\diamond(\Omega)$ be the potential corresponding to the unperturbed conductivity distribution $\sigma_0(x,\omega) \equiv s_0(\omega)$ with the input current f_m, namely

$$\int_\Omega \sigma_0 \nabla v_m \cdot \nabla v\, dx = \int_{\partial\Omega} f_m v\, ds, \qquad v \in H^1(\Omega). \tag{2.4}$$

We observe that $v_m = v_m^*/s_0(\omega)$, where v_m^* is the solution of (2.4) corresponding to the case $s_0 \equiv 1$. In other words, the dependence of v_m on the frequency ω is explicit. By taking $v = v_m$ in (2.3) and $v = u_n$ in (2.4), and subtracting the two identities, we obtain

$$\sum_{k=0}^{K} s_k(\omega) \int_\Omega \delta\sigma_k \nabla u_n \cdot \nabla v_m\, dx = \int_{\partial\Omega} (f_n v_m - f_m u_n)\, ds.$$

Hence, under the approximation $\nabla u_n(x,\omega) \approx \nabla v_n(x,\omega)$ in the domain Ω (valid in the linear regime), and using the identity $v_m = v_m^*/s_0(\omega)$, we arrive at the following linearized model:

$$\sum_{k=0}^{K} s_k(\omega) \int_\Omega \delta\sigma_k \nabla v_n^* \cdot \nabla v_m^* \, dx = s_0(\omega)^2 \int_{\partial\Omega} (f_n v_m - f_m u_n) \, ds. \tag{2.5}$$

The right hand side of the above identity can be treated as a known quantity: u_m is the measured electrode voltage data (and thus depends on the frequency ω), and v_m can be computed (using the reference conductivity $\sigma_0(x,\omega) \equiv s_0(\omega)$). Next, we triangulate the domain Ω into a shape-regular quasi-uniform mesh of simplicial elements $\{\Omega_l\}_{l=1}^L$ such that $\overline{\Omega} = \cup_{l=1}^L \Omega_l$, and consider a piecewise constant approximation of the inclusions $\delta\sigma_k$: for $k = 0, \ldots, K$,

$$\delta\sigma_k(x) \approx \sum_{l=1}^{L} (\delta\sigma_k)_l \chi_{\Omega_l}(x),$$

where χ_{Ω_l} is the characteristic function of the lth element Ω_l, and $(\delta\sigma_k)_l$ denotes the value of the kth abundance $\delta\sigma_k$ in the lth element Ω_l. Substituting the approximation into (2.5), we have the following finite-dimensional linear inverse problem

$$\sum_{k=0}^{K} s_k(\omega) \sum_{l=1}^{L} (\delta\sigma_k)_l \int_{\Omega_l} \nabla v_n^* \cdot \nabla v_m^* \, dx = s_0(\omega)^2 \int_{\partial\Omega} (f_n v_m - f_m u_n) \, ds.$$

Last, we introduce the sensitivity matrix M and the data vector X. We use a single index $j = 1, \ldots, J$ with $J = N^2$ for the index pair (m,n) with $j = N(m-1)+n$, and introduce the sensitivity matrix $M = [M_{jl}] \in \mathbb{R}^{J \times L}$ with its entries M_{jl} given by

$$M_{jl} = \int_{\Omega_l} \nabla v_n^* \cdot \nabla v_m^* \, dx \quad (j \leftrightarrow (m,n)),$$

which is independent of the frequency ω. Likewise, we introduce a data vector $X(\omega) \in \mathbb{R}^J$ with its jth entry $X_j(\omega)$ given by

$$X_j(\omega) = s_0(\omega)^2 \int_{\partial\Omega} (f_n v_m(\omega) - f_m u_n(\omega)) \, ds \quad (j \leftrightarrow (m,n)).$$

Upon writing the vectors $A_k = (\delta\sigma_k)_l \in \mathbb{R}^L$, $k = 0, \ldots, K$, we obtain the following linear system (parameterized by the frequency ω)

$$M \sum_{k=0}^{K} s_k(\omega) A_k = X(\omega). \tag{2.6}$$

In the mfEIT inverse problem, the abundance vectors $\{A_k\}_{k=0}^K$ are of primary interest and have to be estimated from the frequency dependent data $X(\omega)$, and occasionally the spectral profiles $\{s_k(\omega)\}_{k=1}^K$ are also of interest. (Recall that the background spectral profile $s_0(\omega)$ is always supposed to be known.) Depending on the further a priori knowledge available about the spectral profiles $\{s_k(\omega)\}_{k=1}^K$, we distinguish the following three cases:

(a) All the spectral profiles $\{s_k(\omega)\}_{k=0}^K$ are known;

(b) The spectral profiles $\{s_k(\omega)\}_{k=1}^K$ may not be fully known, but their frequency dependence differs substantially;

(c) The spectral profiles are only partially known, and we aim at a partial recovery of the abundances.

These three cases are of different degree of challenge, and we shall discuss them separately below.

2.1 Case (a): Known Spectral Profiles

First we consider the case when the spectral profiles $\{s_k(\omega)\}_{k=0}^K$ are all known. In some applications, this does not represent a restriction, since the spectral profiles of many materials can actually be measured accurately (see e.g. [16] for the electrical conductivity of tissues at frequencies below 1 MHz). Suppose that we can measure $X(\omega)$ at Q distinct frequencies $\{\omega_q\}_{q=1}^Q$. Then by writing $S = (S_{kq}) \in \mathbb{R}^{(K+1)\times Q}$, with $S_{kq} = s_k(\omega_q)$, we get from (2.6) the following matrix equation

$$MAS = X, \tag{2.7}$$

where the matrix $X = [X(\omega_1) \ \dots \ X(\omega_Q)] \in \mathbb{R}^{J\times Q}$. In equation (2.7), the sensitivity matrix M can be precomputed, and the spectral profile matrix S and the data X are known: only the abundance matrix $A = [A_0 \ \dots \ A_K] \in \mathbb{R}^{L\times(K+1)}$ is unknown. It is natural to assume that a sufficiently large number of frequencies are taken, so that the corresponding spectral profile matrix S is incoherent in the sense that $Q \geq K+1$ and $\operatorname{rank}(S) = K+1$ (and presumably S is also well-conditioned). Then the matrix S admits a right inverse S^{-1}. By letting $Y = XS^{-1}$ we obtain

$$MA = Y.$$

These are $K+1$ decoupled (and usually undetermined) linear system. By letting $Y = [Y_0 \ \dots \ Y_K] \in \mathbb{R}^{J\times(K+1)}$, we have $K+1$ independent (finite-dimensional) linear inverse problems

$$MA_k = Y_k, \quad k = 0, \dots, K, \tag{2.8}$$

where A_k represents the kth abundance. Here each linear system determines one and only one abundance A_k. The stable and accurate numerical solution of these ill-conditioned linear systems by suitable regularization techniques will be discussed in detail in Section 5 below.

The condition $\operatorname{rank}(S) = K+1$ on the matrix S is necessary and sufficient for the full decoupling of the abundances, and the well-conditioning of S ensures a stable decoupling procedure. It specifies the condition under which the abundance unmixing is practically feasible, and also the proper selection of the frequencies $\{\omega_q\}_{q=1}^Q$ such that $\operatorname{rank}(S) = K+1$. Note that the condition $\operatorname{rank}(S) = K+1$ depends essentially on the independence/incoherence of the continuous spectral profiles $\{s_k(\omega)\}_{k=0}^K$ (or frequency contrast). In the absence of this spectral incoherence, a full decoupling is impossible. For example, consider the simple case of two endmembers, with $s_0(\omega) = 1+\omega$, $s_1(\omega) = 2+2\omega$. Then no matter how many frequencies one chooses, the spectral matrix S is always of rank one. Thus it is impossible to separate the two abundances, and instead only a linear combination can be obtained.

The right inverse $Y = XS^{-1}$ can alternatively be viewed as a least-squares procedure

$$\min_{Y\in\mathbb{R}^{J\times(K+1)}} \|X - YS\|_F.$$

This formulation exhibits clearly that for a rank-deficient spectral matrix S, the proposed approach yields the minimum-norm matrix Y compatible with the data, and for an inconsistent S, it yields a best approximation via projection (even though the physical interpretation is less clear). In addition, by the perturbation theory for least-squares problems [22], the well-conditioning of the spectral matrix S implies that the procedure is also stable with respect to small perturbations in the spectral profiles.

It is worth noting that this approach represents a natural generalization of the weighted frequency difference EIT (fdEIT) method proposed in [46], where only two abundances and two frequencies are considered ($K = 1$ and $Q = 2$).

Example 1. Consider the case with $K = 1$ and $Q = 2$, namely, two inclusions and two frequencies. We write

$$X = [X(\omega_1) \ X(\omega_2)] \quad \text{and} \quad S = \begin{bmatrix} s_0(\omega_1) & s_0(\omega_2) \\ s_1(\omega_1) & s_1(\omega_2) \end{bmatrix}.$$

Therefore, if S is invertible, we obtain

$$Y = XS^{-1} = \frac{s_0(\omega_1)}{\det S}\left[\frac{s_1(\omega_2)}{s_0(\omega_1)}X(\omega_1) - \frac{s_1(\omega_1)}{s_0(\omega_1)}X(\omega_2) \quad X(\omega_2) - \frac{s_0(\omega_2)}{s_0(\omega_1)}X(\omega_1)\right].$$

The second column of Y recovers exactly the weighted fdEIT method discussed in [46]. Thus our method generalizes [46], as the recent work [32]. Our approach is slightly more general since it directly incorporates the multifrequency data. The use of multiple frequencies is expected to improve the numerical stability, especially when high correlation may occur between neighboring frequencies and possibly the spectral profiles themselves are not precisely known. Further, the use of multiple frequencies enables completely decoupling multiple inclusions, instead of only one inclusion, which can be very useful in practice. It is also worth noting that in the special case of constant background spectral profile $s_0(\omega_1) = s_0(\omega_2)$, the approach reduces to the usual frequency difference. This delineates the region of validity of the usual frequency difference imaging for processing multifrequency data. We also note that the invertibility of the spectral matrix S is equivalent to the fact that the two rows of S are not collinear, i.e., the two frequency profiles are incoherent, and there is frequency dependent conductivity contrast.

2.2 Case (b): Spectral Profiles with Substantially Different Frequency Dependence

Next we consider the case when some of (or, possibly, all) the spectral profiles $\{s_k(\omega)\}_{k=1}^K$ are not known, but do not change rapidly with the frequency ω, when compared to the remaining ones. Thus, instead of using the data $X(\omega)$ directly, it is natural to differentiate the relation (2.6) with respect to ω to eliminate the contributions from the abundances whose endmembers do not vary much with the frequency ω. This discriminating effect is useful in practice. For example, it is known that the conductivity of the malign tissues is more sensitive with respect to frequency variations in certain frequency ranges [49, 39], even though the conductivity of healthy tissues in the background may exhibit fairly complex structure. The differentiation procedure provides a valuable tool in such scenarios.

More precisely, let $\mathcal{P} \subseteq \{0, 1, \ldots, K\}$ be such that

$$\left|\frac{d}{d\omega}s_p(\omega_q)\right| \gg \left|\frac{d}{d\omega}s_k(\omega_q)\right|, \qquad p \in \mathcal{P}, k \in \{0, 1, \ldots, K\} \setminus \mathcal{P}. \tag{2.9}$$

By differentiating (2.6) with respect to the frequency ω we obtain

$$M\sum_{k=0}^{K} A_k \frac{d}{d\omega}s_k(\omega) = \frac{d}{d\omega}X(\omega).$$

In view of the assumption (2.9), this equality may be rewritten as

$$M\sum_{p\in\mathcal{P}} A_p \frac{d}{d\omega}s_p(\omega) \approx \frac{d}{d\omega}X(\omega). \tag{2.10}$$

In other words, the contributions from the remaining profiles are negligible, provided that the abundances A_k are comparable in magnitude. Different reconstruction schemes should be used depending on whether the spectral profiles $\{s_p(\omega)\}_{p\in\mathcal{P}}$ are known.

2.2.1 Case (b1): The Spectral Profiles $\{s_p(\omega)\}_{p\in\mathcal{P}}$ are not Known

In the case when the spectral profiles $\{s_p(\omega)\}_{p\in\mathcal{P}}$ are not known, the linear system (2.10) cannot be simplified further. By solving this underdetermined system, we can recover at most $\sum_{p\in\mathcal{P}} s'_p(\omega)A_p$, namely a linear combination of the inclusions. Since the weights $\{s'_p(\omega)\}_{p\in\mathcal{P}}$ are unknown, it is impossible to separate the abundances $\{A_p, p \in \mathcal{P}\}$. However, in the particular case when $\mathcal{P} = \{p\}$ (i.e., $|\mathcal{P}| = 1$),

the abundance $\delta\sigma_p$ may be recovered up to an unknown multiplicative constant, which gives the support information.

We illustrate the technique with an example.

Example 2. Consider the case $K = 1$, and two linear frequency profiles, i.e.,

$$s_0(\omega) = \alpha_0 + \beta_0\omega \quad \text{and} \quad s_1(\omega) = \alpha_1 + \beta_1\omega,$$

with $\beta_0 \ll \beta_1$. Then the differentiation imaging amounts to

$$\beta_0 MA_0 + \beta_1 MA_1 = X'(\omega).$$

If MA_0 and MA_1 are comparable, then $\beta_0 \ll \beta_1$ implies that the contribution of $\beta_0 MA_0$ to the data is negligible (in comparison with $\beta_1 MA_1$). Hence, upon differentiation, the technique allows to recover the dominant component $\beta_1 MA_1$, which upon linear inversion yields $\beta_1 A_1$. In particular, this contains the support information about the abundance A_1, and also its magnitude up to a multiplicative constant. Further, for known β_1, it allows full recovery of the abundance A_1.

2.2.2 Case (b2): The Spectral Profiles $\{s_p(\omega)\}_{p\in\mathcal{P}}$ are Known

If the spectral profiles $\{s_p(\omega)\}_{p\in\mathcal{P}}$ are known, it is possible to perform the same analysis of Case (a) (in Section 2.1) to system (2.10). Taking measurements at Q distinct frequencies $\omega_1, \ldots, \omega_Q$, we have

$$M \sum_{p\in\mathcal{P}} A_p s_p'(\omega_q) \approx X'(\omega_q), \qquad q = 1, \ldots, Q.$$

Then, by writing $\widetilde{S} = (\widetilde{S}_{pq}) \in \mathbb{R}^{|\mathcal{P}|\times Q}$, with $\widetilde{S}_{pq} = s_p'(\omega_q)$, we get

$$MA\widetilde{S} = X'$$

where the matrix $X' = [X'(\omega_1) \ \ldots \ X'(\omega_Q)] \in \mathbb{R}^{J\times Q}$. Then the inversion step is completely analogous to that discussed in Section 2.1, provided that the incoherence condition $\operatorname{rank} \widetilde{S} = |\mathcal{P}|$ (as well as well-conditioning) holds. All the inclusions A_p, $p \in \mathcal{P}$, can be recovered.

2.2.3 Numerical Implementation

In the implementation, we take the forward difference between neighboring frequencies

$$M \sum_{k=0}^{K} A_k \frac{s_k(\omega_{q+1}) - s_k(\omega_q)}{\omega_{q+1} - \omega_q} = \frac{X(\omega_{q+1}) - X(\omega_q)}{\omega_{q+1} - \omega_q}. \tag{2.11}$$

It approximates the first order derivative $s_k'(\omega_q)$ with the forward difference

$$\frac{d}{d\omega} s_k(\omega_q) \approx \frac{s_k(\omega_{q+1}) - s_k(\omega_q)}{\omega_{q+1} - \omega_q}.$$

If more than one neighboring frequencies are available, it is also possible to use higher order difference formulas to get more accurate approximations of the derivative $s_k'(\omega)$, e.g., central difference scheme (on a nonuniform frequency grid)

$$\frac{d}{d\omega} s_k(\omega_q) \approx \frac{\delta\omega_{q-1}^2 (s_k(\omega_{q+1}) - s_k(\omega_q)) + \delta\omega_q^2 (s_k(\omega_q) - s_k(\omega_{q-1}))}{\delta\omega_q \delta\omega_{q-1} (\delta\omega_q + \delta\omega_{q-1})},$$

where $\delta\omega_q = \omega_{q+1} - \omega_q$. In practice, these represent different ways to perform differentiation imaging. However, their robustness with respect to noise in the data might differ due to the well-known ill-posed nature of numerical differentiation [24]. In this work, we shall use the forward difference scheme (2.11).

2.3 Case (c): Partially Known Spectral Profiles, Partial Recovery of the Abundances

In practice, it is also of interest to recover some information about the abundances when the spectral profiles $\{s_k(\omega)\}$ are only partially known. Unfortunately, in general, this is infeasible. But, one can still obtain some information under certain a priori knowledge. To discuss the situation, recall the notation $Y_k = MA_k$, cf. (2.8). Then

$$Y_0 s_0(\omega_q) + \ldots + Y_K s_K(\omega_q) = X(\omega_q), \qquad q = 1, \ldots, Q. \tag{2.12}$$

Now suppose the frequency dependence of the spectral profiles $\{s_k(\omega)\}_{k=0}^K$ are of polynomial type, namely

$$s_k(\omega) = \sum_{n=0}^{N} \alpha_k^n \omega^n.$$

Inserting this expression in the identity (2.12) yields

$$\sum_{n=0}^{N} \sum_{k=0}^{K} (\alpha_k^n Y_k) \omega^n = X(\omega).$$

By taking a sufficiently large number of modulating frequencies $\{\omega_q\}_{q=1}^Q$, and using the identity principle for polynomials, we can compute the quantities

$$B_n := \sum_{k=0}^{K} \alpha_k^n Y_k, \qquad n = 0, \ldots, N.$$

Note that adding more frequencies would not add more information about Y_k and α_k^j than $\{B_n\}_{n=0}^N$. In other words, the quantities $\{B_n\}_{n=0}^N$ represent the essential information content in the data $\{X(\omega_q)\}_{q=1}^Q$ about the unknowns $\{Y_k\}_{k=0}^K$ and $\{\alpha_k^n : k = 0, \ldots, K,\ n = 0, \ldots, N\}$. Depending on K, N and the number of unknowns among the weights α_k^n of the spectral profiles, some inclusions Y_k can be reconstructed without knowing the corresponding spectral profiles. In other situations, there may be more unknowns than the number of equations, and it may be infeasible to determine all of them.

Instead of providing a general analysis of all possible cases, we present two examples that explain the different situations that may appear.

Example 3. Consider the case $K = 1$. For every n we have $B_0 = \alpha_0^0 Y_0 + \alpha_1^0 Y_1$ and $B_n = \alpha_0^n Y_0 + \alpha_1^n Y_1$, whence

$$Y_1 = (\alpha_0^0 \alpha_1^n - \alpha_1^0 \alpha_0^n)^{-1} (\alpha_0^0 B_n - \alpha_0^n B_0).$$

Since the spectral profile s_0 is always assumed to be known, so are the quantities α_0^0 and α_0^n. Therefore, Y_1 may be reconstructed up to a multiplicative constant c, provided that $\alpha_0^0 \alpha_1^n - \alpha_1^0 \alpha_0^n \neq 0$, without assuming any knowledge of the corresponding spectral profile s_1. Note that this nonzero condition simply represents the incoherence of the spectral profiles s_0 and s_1. Finally, by solving the underdetermined system $MA_1 = cY_1$, the inclusion $\delta\sigma_1$ can be reconstructed up to the multiplicative constant c.

In addition, assuming a unique recovery of the linearized EIT inverse problem, the knowledge of the quantity B_0 allows to recover an unknown linear combination of the abundances A_0 and A_1, and in particular the union of their supports. Since the supports of A_0 and A_1 are assumed to be disjoint from each other, this piece of information allows the support of the abundance A_0 to be recovered, given that the support of the abundance A_1 has already been reconstructed.

Example 4. Note that if $K = 2$ and $N = 1$, we get only

$$\alpha_0^0 Y_0 + \alpha_1^0 Y_1 + \alpha_2^0 Y_2 = B_0 \quad \text{and} \quad \alpha_0^1 Y_0 + \alpha_1^1 Y_1 + \alpha_2^1 Y_2 = B_1,$$

which is vastly insufficient to determine all the unknowns. However, a calculation similar to the one presented in the previous example shows that Y_2 can be determined up to a multiplicative constant if $K = N = 2$ and s_1 is known, provided that a certain nonzero condition is satisfied. Like before, by solving the underdetermined system $MA_2 = cY_2$, we can reconstruct the inclusion $\delta\sigma_2$ up to a multiplicative constant, and in particular its support. Thus, assuming a unique recovery with the linearized inverse problem, the union of the supports of $\delta\sigma_0$ and $\delta\sigma_1$ may be determined.

With obvious modifications, the preceding discussion is also valid for more general basis functions $\phi_n(\omega)$ which form a unisolvent system on the set of measured frequencies $\{\omega_q\}_{q=1}^{Q}$ [15, pp. 31–32].

3 Imperfectly Known Boundary

In this part, we illustrate the significant potentials of mfEIT for handling modelling errors, as in the case of an imperfectly known boundary. The analysis may be extended to other interesting scenarios, including imperfectly known contact impedances or injected currents. Here we shall discuss only the case of an imperfectly known boundary. This has long been one of the main obstacles in some practical applications of the EIT imaging [2, 36, 37]. It is known that the use of a slightly incorrect boundary can lead to significant errors in the reconstruction. mfEIT was proposed as one promising strategy to partially overcome the challenge in [46], where its potential was also numerically demonstrated. Here we shall present an analysis of the approach in the linearized regime which justifies these numerical findings.

We denote the true but unknown physical domain by $\widetilde{\Omega}$, and the computational domain by Ω, which is an approximation of $\widetilde{\Omega}$. Next we introduce a forward map $F : \widetilde{\Omega} \to \Omega$, $\widetilde{x} \to x$, which is assumed to be a smooth orientation preserving map with a sufficiently smooth inverse map $F^{-1} : \Omega \to \widetilde{\Omega}$. We denote the Jacobian of the map F by J_F, and the Jacobian of F with respect to the surface integral by J_F^S.

Suppose now that the function $\widetilde{u}_n(\widetilde{x}, \omega)$ satisfies problem (2.1) in the true domain $\widetilde{\Omega}$ with a conductivity $\widetilde{\sigma}(\widetilde{x}, \omega)$ and input current $\widetilde{f}_n$ on $\partial\widetilde{\Omega}$ with $\int_{\partial\widetilde{\Omega}} \widetilde{f}_n \, ds = 0$, namely

$$\begin{cases} -\nabla_{\widetilde{x}} \cdot (\widetilde{\sigma}(\widetilde{x}, \omega)\nabla_{\widetilde{x}}\widetilde{u}_n(\widetilde{x}, \omega)) = 0 \quad \text{in } \widetilde{\Omega}, \\ \widetilde{\sigma}(\widetilde{x}, \omega)\dfrac{\partial\widetilde{u}_n(\widetilde{x}, \omega)}{\partial\widetilde{\nu}} = \widetilde{f}_n \quad \text{on } \partial\widetilde{\Omega}, \\ \displaystyle\int_{\partial\widetilde{\Omega}} \widetilde{u}_n(\widetilde{x}, \omega) d\widetilde{s} = 0. \end{cases} \tag{3.1}$$

Here the frequency-dependent conductivity $\widetilde{\sigma}(\widetilde{x}, \omega)$ takes a separable form (cf. (2.2))

$$\widetilde{\sigma}(\widetilde{x}, \omega) = \sum_{k=0}^{K} s_k(\omega)\widetilde{\sigma}_k(\widetilde{x}), \tag{3.2}$$

with $\widetilde{\sigma}_0(\widetilde{x}) = 1 + \delta\widetilde{\sigma}_0(\widetilde{x})$, and $\widetilde{\sigma}_k(\widetilde{x}) = \delta\widetilde{\sigma}_k(\widetilde{x})$, $k = 1, \ldots, K$, where $\delta\widetilde{\sigma}_k$ are small and their supports are disjoint and stay away from the boundary $\partial\widetilde{\Omega}$. The weak formulation of problem (3.1) (by suppressing the dependence on the frequency ω) is given by: find $\widetilde{u}_n(\cdot, \omega) \in H^1(\widetilde{\Omega})$ with $\int_{\partial\widetilde{\Omega}} \widetilde{u}_n(\widetilde{x}, \omega) d\widetilde{s} = 0$ such that

$$\int_{\widetilde{\Omega}} \widetilde{\sigma}(\widetilde{x})\nabla_{\widetilde{x}}\widetilde{u}_n(\widetilde{x}) \cdot \nabla_{\widetilde{x}}\widetilde{v}(\widetilde{x}) d\widetilde{x} = \int_{\partial\widetilde{\Omega}} \widetilde{f}_n \widetilde{v} d\widetilde{s}, \qquad \widetilde{v} \in H^1(\widetilde{\Omega}). \tag{3.3}$$

Let us now discuss the experimental setup. The practitioner chooses a current density defined on the computational domain Ω, namely a function $f_n \in L^2_\diamond(\partial\Omega)$. This current is then applied to the unknown boundary $\partial\widetilde{\Omega}$ of the real domain $\widetilde{\Omega}$. The deformation of the boundary has to be taken into account: the applied current $\widetilde{f}_n$ on $\partial\widetilde{\Omega}$ results to be

$$\widetilde{f}_n = (f_n \circ F)|\det J_F^S|. \tag{3.4}$$

This implies directly $\int_{\partial\widetilde{\Omega}} \widetilde{f}_n d\widetilde{s} = 0$, which ensures the well-posedness of problem (3.1) or equivalently (3.3). This induces the electric potential $\widetilde{u}_n \in H^1(\widetilde{\Omega})$ given by (3.3). Like in Section 2, the electric potential $\widetilde{u}_n$ is assumed to be measured on $\partial\widetilde{\Omega}$. However, because of the incorrect knowledge of the boundary, the measured quantity is in fact $u_n := \widetilde{u}_n \circ F^{-1}$ restricted to the computational boundary $\partial\Omega$.

Remark 1. The factor $|\det J_F^S|$ in (3.4) has a physical interpretation. The current density on $\partial\widetilde{\Omega}$ is locally defined by $\widetilde{J} = I/\mathrm{area}(\widetilde{A})$, where I is the current injected through a small surface $\widetilde{A} \subseteq \partial\widetilde{\Omega}$. Thus

$$\widetilde{J} = \frac{I}{\mathrm{area}(\widetilde{A})} = \frac{I}{\mathrm{area}(A)} \frac{\mathrm{area}(A)}{\mathrm{area}(\widetilde{A})} = J \frac{\mathrm{area}(A)}{\mathrm{area}(\widetilde{A})},$$

where J is the corresponding current density on $A := F(\widetilde{A}) \subseteq \partial\Omega$. Therefore, the factor $|\det J_F^S|$ is nothing other than the infinitesimal version of $\frac{\mathrm{area}(A)}{\mathrm{area}(\widetilde{A})}$ as $\mathrm{area}(\widetilde{A}) \to 0$. It is worth pointing out that the following relation holds trivially true:

$$\int_{\partial\widetilde{\Omega}} \widetilde{f}_n \widetilde{u}_n d\widetilde{s} = \int_{\partial\Omega} f_n u_n \, ds.$$

In physical terms, the integral $\int_{\partial\Omega} f_n u_n \, ds$ represents the power needed to maintain the potential u_n on the boundary $\partial\Omega$. In other words, the choice (3.4) preserves the needed power for the measured data, and it agrees with the one adopted in [36].

We shall consider only the case that the computational domain Ω is a small variation of the true physical domain $\widetilde{\Omega}$ (but comparable with the inclusions $\delta\sigma_k$), so that the linearized regime is valid. Specifically, we write the map $F : \widetilde{\Omega} \to \Omega$ by $F(\widetilde{x}) = \widetilde{x} + \varepsilon\widetilde{\phi}(\widetilde{x})$, where ε is a small scalar parameter and the smooth function $\widetilde{\phi}(\widetilde{x})$ characterizes the domain deformation. Further, let $F^{-1}(x) = x + \varepsilon\phi(x)$ be the inverse map, which is also smooth.

To examine the influences of the domain deformation on the linearized inverse problem discussed in Section 2, we introduce the solution $v_m \in H^1_\diamond(\Omega)$ relative to the reference conductivity distribution $\sigma_0(x,\omega) = s_0(\omega)$ in the computational domain Ω corresponding to the flux f_m, i.e.,

$$\int_\Omega \sigma_0 \nabla v_m \cdot \nabla v \, dx = \int_{\partial\Omega} f_m v \, ds, \qquad v \in H^1(\Omega), \tag{3.5}$$

which is computable over the computational domain Ω.

We can now state the corresponding linearized inverse problem. As a byproduct of the proof, we have that, even for an isotropic conductivity $\widetilde{\sigma}$ in the true domain $\widetilde{\Omega}$, cf. (3.2), in the computational domain Ω the equivalent conductivity $\sigma(x,\omega)$ is generally anisotropic (or matrix valued).

Proposition 1. *Set $\delta\sigma_k = \delta\widetilde{\sigma}_k \circ F^{-1}$ for $k = 0, 1, \ldots, K$ and $v_m^* = s_0(\omega) v_m$ for $m = 1, \ldots, N$. The linearized inverse problem on the computational domain Ω is given by*

$$s_0(\omega)\varepsilon \int_\Omega \Psi \nabla v_n^* \cdot \nabla v_m^* \, dx + \sum_{k=0}^{K} s_k(\omega) \int_\Omega \delta\sigma_k \nabla v_n^* \cdot \nabla v_m^* \, dx = s_0(\omega)^2 \int_{\partial\Omega} (f_n v_m - f_m u_n) \, ds, \tag{3.6}$$

for some smooth function $\Psi : \Omega \to \mathbb{R}^{d\times d}$, which is independent of the frequency ω.

Proof. First, we derive the governing equation for the variable $u_n = \widetilde{u}_n \circ F^{-1}$ in the domain Ω from (3.3). Denote by $v = \widetilde{v} \circ F^{-1} \in H^1(\Omega)$. By the chain rule we have $\nabla_{\widetilde{x}} \widetilde{u}_n \circ F^{-1} = (J_F^t \circ F^{-1}) \nabla_x u_n$, where the superscript t denotes the matrix transpose. Thus, we deduce

$$\begin{aligned}
\int_{\widetilde{\Omega}} \widetilde{\sigma}(\widetilde{x}) \nabla_{\widetilde{x}} \widetilde{u}_n(\widetilde{x}) \cdot \nabla_{\widetilde{x}} \widetilde{v}(\widetilde{x}) d\widetilde{x} &= \int_\Omega (\widetilde{\sigma} \circ F^{-1})(x) (J_F^t \circ F^{-1})(x) \nabla u_n(x) \cdot (J_F^t \circ F^{-1})(x) \nabla v(x) |\det J_{F^{-1}}(x)| dx \\
&= \int_\Omega (J_F \circ F^{-1})(x) (\widetilde{\sigma} \circ F^{-1})(x) (J_F^t \circ F^{-1})(x) \nabla u_n(x) \cdot \nabla v(x) |\det J_{F^{-1}}(x)| dx \\
&= \int_\Omega \sigma(x,\omega) \nabla u_n(x) \cdot \nabla v(x) \, dx,
\end{aligned}$$

where the transformed conductivity $\sigma(x,\omega)$ is given by [50, 36, 37]

$$\sigma(x,\omega) = \left(\frac{J_F(\cdot)\widetilde{\sigma}(\cdot,\omega)J_F^t(\cdot)}{|\det J_F(\cdot)|} \circ F^{-1} \right)(x). \tag{3.7}$$

Moreover, by (3.4) we have $\int_{\partial\widetilde{\Omega}} \widetilde{f}_n \widetilde{v} d\widetilde{s} = \int_{\partial\Omega} f_n v \, ds$. Therefore, in view of (3.3) the potential u_n satisfies

$$\int_\Omega \sigma(x,\omega)\nabla u_n(x,\omega)\cdot\nabla v(x)\,dx = \int_{\partial\Omega} f_n v \, ds, \qquad v \in H^1(\Omega). \tag{3.8}$$

Then by choosing $v = v_m$ in (3.8) and $v = u_n$ in (3.5), we arrive at

$$\int_\Omega (\sigma - \sigma_0)\nabla u_n \cdot \nabla v_m \, dx = \int_{\partial\Omega} (f_n v_m - f_m u_n)\, ds. \tag{3.9}$$

Note that $J_F = I + \varepsilon J_{\widetilde{\phi}}$, and $J_{F^{-1}} = I + \varepsilon J_\phi = I - \varepsilon J_{\widetilde{\phi}} \circ F^{-1} + O(\varepsilon^2)$, since ε is small. It is known that $|\det J_F| = 1 + \varepsilon \mathrm{div}\widetilde{\phi} + O(\varepsilon^2)$ [25, equation (2.10)]. Then the transformed conductivity $\sigma(x,\omega)$ can be explicitly written as

$$\begin{aligned}
\sigma(x,\omega) &= \widetilde{\sigma}(\cdot,\omega)(1+\varepsilon \mathrm{div}\widetilde{\phi}(\cdot))^{-1}(I + \varepsilon(J_{\widetilde{\phi}}(\cdot) + J_{\widetilde{\phi}}^t(\cdot))) \circ F^{-1}(x) + O(\varepsilon^2) \\
&= \widetilde{\sigma}(\cdot,\omega)((1-\varepsilon \mathrm{div}\widetilde{\phi}(\cdot))I + \varepsilon(J_{\widetilde{\phi}}(\cdot) + J_{\widetilde{\phi}}^t(\cdot))) \circ F^{-1}(x) + O(\varepsilon^2) \\
&= \widetilde{\sigma}(\cdot,\omega) \circ F^{-1}(x) + \Psi(x)\varepsilon + O(\varepsilon^2).
\end{aligned}$$

where $\Psi = (J_{\widetilde{\phi}} + J_{\widetilde{\phi}}^t - \mathrm{div}\widetilde{\phi} I) \circ F^{-1}$ is smooth and independent of the frequency ω. Upon collecting terms, this together with the separable form of $\widetilde{\sigma}(\widetilde{x},\omega)$ in (3.2) yields

$$\sigma(x,\omega) \approx s_0(\omega) I + \varepsilon s_0(\omega)\Psi(x) + \sum_{k=0}^{K} \delta\sigma_k(x) s_k(\omega) I. \tag{3.10}$$

Upon substituting it into (3.9) and invoking the approximation $\nabla u_n \approx \nabla v_n$ in the domain, we obtain the desired expression. □

By Proposition 1, in the presence of an imperfectly known boundary with the deformation magnitude ε comparable with the inclusions $\{\delta\sigma_k\}_{k=0}^K$, there is a dominant source of errors in the linearized inverse problem: the perturbed sensitivity system contains an additional anisotropic component $\varepsilon\Psi$, resulting from the domain deformation. As a consequence, a direct inversion of the linearized model (3.6) is unsuitable. This is consistent with the empirical observation that a slightly incorrect boundary can lead to completely erroneous reconstructions [2, 21].

This issue can be resolved by using the proposed multifrequency approach. Indeed, by rearranging the terms in (3.6) we obtain

$$s_0(\omega)\int_\Omega (\varepsilon\Psi + \delta\sigma_0)\nabla v_n^* \cdot \nabla v_m^* \, dx + \sum_{k=1}^{K} s_k(\omega) \int_\Omega \delta\sigma_k \nabla v_n^* \cdot \nabla v_m^* \, dx = s_0(\omega)^2 \int_{\partial\Omega} (f_n v_m - f_m u_n)\, ds. \tag{3.11}$$

This equation is completely analogous to (2.5), with the only difference lying in the additional term $\varepsilon\Psi$. Therefore, all the methods discussed in Section 2 may be applied straightforwardly, since the right hand side is known. The background perturbation $\delta\sigma_0$ will never be properly reconstructed, due to the pollution of the error term $\varepsilon\Psi$. However, the inclusions corresponding to the other frequency profiles may be reconstructed, since they are affected by the deformation only through $\delta\sigma_k = \delta\widetilde{\sigma}_k \circ F^{-1}$. In other words, the location and shape can be slightly deformed. Thus we have shown that mfEIT is a very effective method to eliminate the modelling errors caused by the boundary uncertainty. Only the background anomaly (i.e., the inclusion $\delta\sigma_0$) is affected, and so cannot be reconstructed. All the other inclusions may be imaged successfully.

4 The Complete Electrode Model

In this section we adapt the approach discussed in Sections 2 and 3 to the more realistic complete electrode model, which has been shown to reproduce the experimental data within measurement precision [13] and is currently regarded as the most accurate model in a number of applications. We discuss the cases of a perfectly known and an imperfectly known boundary separately.

4.1 Perfectly Known Boundary

First we consider the case of a perfectly known boundary. Let Ω be an open bounded domain in $\mathbb{R}^d$ ($d = 2, 3$), with a smooth boundary $\partial\Omega$. We denote the set of electrodes by $\{e_j\}_{j=1}^E \subset \partial\Omega$, which are disjoint from each other, i.e., $\bar{e}_i \cap \bar{e}_k = \emptyset$ if $i \neq k$. The applied current on the jth electrode e_j is denoted by I_j, and the current vector $I = (I_1, \ldots, I_E)^t$ satisfies $\sum_{j=1}^E I_j = 0$ by the law of charge conservation. Let the space $\mathbb{R}^E_\diamond$ be the subspace of the vector space $\mathbb{R}^E$ with zero mean, i.e., $I \in \mathbb{R}^E_\diamond$. The electrode voltages $U = (U_1, \ldots, U_E)^t$ are also normalized so that $U \in \mathbb{R}^E_\diamond$. Then the mathematical formulation of the complete electrode model (CEM) reads [13, 48]: given the frequency-dependent conductivity distribution $\sigma(x, \omega)$, positive contact impedances $\{z_j\}_{j=1}^E$ and an input current pattern $I \in \mathbb{R}^E_\diamond$, find the potential $u(\cdot, \omega) \in H^1(\Omega)$ and the electrode voltages $U \in \mathbb{R}^E_\diamond$ such that

$$\begin{cases} -\nabla \cdot (\sigma(x,\omega)\nabla u(x,\omega)) = 0 \text{ in } \Omega, \\ \qquad u + z_j \dfrac{\partial u}{\partial \nu_\sigma} = U_j \text{ on } e_j,\ j = 1, 2, \ldots, E, \\ \displaystyle\int_{e_j} \frac{\partial u}{\partial \nu_\sigma}\, ds = I_j \text{ for } j = 1, 2, \ldots, E, \\ \qquad \dfrac{\partial u}{\partial \nu_\sigma} = 0 \text{ on } \partial\Omega \backslash \cup_{j=1}^E e_j, \end{cases} \tag{4.1}$$

where $\frac{\partial u}{\partial \nu_\sigma}$ denotes the co-normal derivative $(\sigma\nabla u) \cdot \nu$. The second line describes the contact impedance effect: when injecting electrical currents into the object, a highly resistive thin layer forms at the electrode-electrolyte interface (due to certain electrochemical processes), which causes potential drops across this interface. The potential drop is described by Ohm's law, with the positive constants $\{z_j\}_{j=1}^E$ being contact impedances. In practice, it was observed that the contact impedances $\{z_j\}_{j=1}^E$ are inversely proportional to the conductivity of the object [28, 30], and thus we can write

$$z_j = s_0(\omega)^{-1} c_j, \tag{4.2}$$

for some constants $c_j > 0$ independently of the frequency, since by assumption, near the boundary $\partial\Omega$ we have $\sigma(x, \omega) = s_0(\omega)$. The metallic electrodes are perfect conductors, and hence the voltage U_j on the jth electrode e_j is a constant. The weak formulation of model (4.1) is given by: find $(u, U) \in \mathbb{H} := H^1(\Omega) \times \mathbb{R}^E_\diamond$ (equipped with the product norm) such that [48]

$$\int_\Omega \sigma(x,\omega)\nabla u(x,\omega) \cdot \nabla v(x)\, dx + \sum_{j=1}^E z_j^{-1} \int_{e_j} (u - U_j)(v - V_j)\, ds = \sum_{j=1}^E I_j U_j, \qquad (v, V) \in \mathbb{H}.$$

The bilinear form defined on the left hand side is coercive and continuous on the space $\mathbb{H}$, and thus by Lax-Milgram theorem there exists a unique solution $(u(\cdot, \omega), U(\omega)) \in \mathbb{H}$.

Consider N input currents $\{I_n\}_{n=1}^N \subset \mathbb{R}^E_\diamond$, and let $\{(u_n, U_n)\}_{n=1}^N \subset \mathbb{H}$ be the corresponding solutions to the complete electrode model (4.1), i.e.,

$$\int_\Omega \sigma(x,\omega)\nabla u_n(x,\omega) \cdot \nabla v(x,\omega)\, dx + \sum_{j=1}^E z_j^{-1} \int_{e_j} (u_n - U_{n,j})(v - V_j)\, ds = \sum_{j=1}^E I_{n,j} V_j, \qquad (v, V) \in \mathbb{H}. \tag{4.3}$$

The electrode voltages $U_n \in \mathbb{R}^E_\diamond$ can be measured in practice, and are used to recover the conductivity distribution $\sigma(x,\omega)$. To derive a linearized model, like before, let $(v_m, V_m) \in \mathbb{H}$ be the solution corresponding to the unperturbed conductivity field with $\sigma_0(x,\omega) = s_0(\omega)$:

$$\int_\Omega \sigma_0(x,\omega)\nabla v_m(x,\omega)\cdot\nabla v(x,\omega)\,dx + \sum_{j=1}^E z_j^{-1}\int_{e_j}(v_m - V_{m,j})(v - V_j)\,ds = \sum_{j=1}^E I_{m,j}V_j, \qquad (v,V)\in\mathbb{H}. \quad (4.4)$$

Like in the continuum model, in view of the relation (4.2), we can write $(v_m^*, V_m^*) = s_0(\omega)(v_m, V_m)$ for the solution corresponding to the case $\sigma_0 \equiv 1$. Now we assume that the conductivity $\sigma(x,\omega)$ follows the separable form (2.2). Using the weak formulations for (u_n, U_n) and (v_m, V_m), we deduce immediately

$$\sum_{k=0}^K s_k(\omega)\int_\Omega \delta\sigma_k(x)\nabla u_n(x,\omega)\cdot\nabla v_m(x,\omega)\,dx = \sum_{j=1}^E (I_{n,j}V_{m,j} - I_{m,j}U_{n,j}).$$

Then, under the approximation $\nabla u_n \approx \nabla v_n$ in the domain Ω, and the piecewise constant approximation on the inclusions $\delta\sigma_k$s on the quasi-uniform triangulation $\{\Omega_l\}_{l=1}^L$ of the domain Ω, we have

$$\sum_{k=0}^K s_k(\omega)\sum_{l=1}^L (\delta\sigma_k)_l \int_{\Omega_l}\nabla v_n^*\cdot\nabla v_m^*\,dx = s_0(\omega)^2\sum_{j=1}^E (I_{n,j}V_{m,j} - I_{m,j}U_{n,j}).$$

This formula is almost identical with that for the continuum model, cf. (2.5), and formally their only difference lies in the computation of the data vector $X(\omega)$. Hence, all the discussions in Section 2 can be adapted straightforwardly to the complete electrode model (4.1). In particular, all inversion methods discussed there can be directly applied to this case.

4.2 Imperfectly Known Boundary

Now we consider the case of an imperfectly known boundary. As in Section 3, let $\widetilde{\Omega}$ be the unknown true domain with a smooth boundary $\partial\widetilde{\Omega}$, and Ω be the computational domain with a smooth boundary $\partial\Omega$. Accordingly, let $\{\widetilde{e}_j\}_{j=1}^E \subset \partial\widetilde{\Omega}$ and $\{e_j\}_{j=1}^E \subset \partial\Omega$ be the real and computational electrodes, respectively and assume they satisfy the usual conditions discussed above. Then we introduce a sufficiently smooth orientation preserving forward map $F : \widetilde{\Omega} \to \Omega$, with a sufficiently smooth inverse $F^{-1} : \Omega \to \widetilde{\Omega}$, and we denote the restriction of F to the boundary $\partial\widetilde{\Omega}$ by $f : \partial\widetilde{\Omega} \to \partial\Omega$. We write $F^{-1}(x) = x + \varepsilon\phi(x)$, where $\varepsilon > 0$ denotes the magnitude of the domain deformation. For simplicity, further, it is assumed that there is no further electrode movement apart from domain deformation, i.e., $e_j = f(\widetilde{e}_j)$, $j = 1,\dots,E$. With the frequency-dependent conductivity $\widetilde{\sigma}(\widetilde{x},\omega)$ of the separable form (3.2) and input current $I_n \in \mathbb{R}^E_\diamond$, by (4.1), the quantity $(\widetilde{u}_n(\widetilde{x},\omega), \widetilde{U}_n(\omega)) \in \widetilde{\mathbb{H}} \equiv H^1(\widetilde{\Omega})\times\mathbb{R}^E_\diamond$ satisfies

$$\begin{cases} -\nabla_{\widetilde{x}}\cdot(\widetilde{\sigma}(\widetilde{x},\omega)\nabla_{\widetilde{x}}\widetilde{u}_n(\widetilde{x},\omega)) = 0 \quad \text{in } \widetilde{\Omega}, \\ \displaystyle\int_{\widetilde{e}_j}\frac{\partial\widetilde{u}_n}{\partial\widetilde{\nu}_{\widetilde{\sigma}}}d\widetilde{s} = I_{n,j} \quad \text{on } \widetilde{e}_j, j = 1,2,\dots,E, \\ \displaystyle z_j\frac{\partial\widetilde{u}_n}{\partial\widetilde{\nu}_{\widetilde{\sigma}}} + \widetilde{u}_n = \widetilde{U}_{n,j} \quad \text{on } \widetilde{e}_j, j = 1,2,\dots,E \\ \displaystyle\frac{\partial\widetilde{u}_n}{\partial\widetilde{\nu}_{\widetilde{\sigma}}} = 0 \quad \text{on } \partial\widetilde{\Omega}\setminus\cup_{j=1}^E\widetilde{e}_j, \end{cases} \quad (4.5)$$

The weak formulation of the problem is given by: find $(\widetilde{u}_n(\widetilde{x},\omega), \widetilde{U}_n(\omega)) \in \widetilde{\mathbb{H}}$ such that

$$\int_{\widetilde{\Omega}}\widetilde{\sigma}(\widetilde{x},\omega)\nabla_{\widetilde{x}}\widetilde{u}_n(\widetilde{x},\omega)\cdot\nabla_{\widetilde{x}}\widetilde{v}(\widetilde{x})d\widetilde{x} + \sum_{j=1}^E z_j^{-1}\int_{\widetilde{e}_j}(\widetilde{u}_n(\widetilde{x},\omega) - \widetilde{U}_{n,j}(\omega))(\widetilde{v}(\widetilde{x}) - \widetilde{V}_j)d\widetilde{s} = \sum_{j=1}^E I_{n,j}\widetilde{V}_j, \quad (\widetilde{v},\widetilde{V})\in\widetilde{\mathbb{H}}.$$

In the experimental setting, on the computational domain Ω, the injected current $I_n \in \mathbb{R}^E$ on the electrodes $\{e_j\}_{j=1}^E$ is known, and the corresponding voltage $\widetilde{U}_n(\omega) \in \mathbb{R}^E$ can be measured. The inverse problem is to recover the inclusion profiles $\{\delta\widetilde{\sigma}_k\}_{k=0}^K$ from the measured electrode voltages $\{\widetilde{U}_n(\omega)\}_{n=1}^N$ at a number of frequencies $\{\omega_q\}_{q=1}^Q$.

Now we can state the corresponding linearized inverse problem for the complete electrode model with an imperfectly known boundary. Consider the potential $u_n(\cdot,\omega) = \widetilde{u}_n(\cdot,\omega) \circ F^{-1}$, and the associated electrode voltages $U_n = \widetilde{U}_n$.

Proposition 2. *Let the reference solutions $(v_m, V_m) \in \mathbb{H}$ be defined by (4.4) and the conductivity $\widetilde{\sigma}$ be of the form (3.2). Set $z = |\det J_{F^{-1}}^S|$, $\delta\sigma_k = \delta\widetilde{\sigma}_k \circ F^{-1}$ for $k = 0, 1, \ldots, K$ and $(v_m^*, V_m^*) = s_0(\omega)(v_m, V_m)$ for $m = 1, \ldots, N$. The linearized inverse problem on the computational domain Ω is given by*

$$s_0(\omega)\varepsilon \int_\Omega \Psi \nabla v_n^* \cdot \nabla v_m^* \, dx + \sum_{k=0}^K s_k(\omega) \int_\Omega \delta\sigma_k \nabla v_n^* \cdot \nabla v_m^* \, dx$$
$$= s_0(\omega)^2 \sum_{j=1}^E (I_{n,j} V_{m,j} - I_{m,j} U_{n,j}) - s_0(\omega) \sum_{j=1}^E c_j \int_{e_j} (z-1) \left(\frac{\partial v_m^*}{\partial \nu} \right)^2 ds, \quad (4.6)$$

for some smooth function $\Psi : \Omega \to \mathbb{R}^{d\times d}$, which is independent of the frequency ω.

Proof. Proceeding as in the proof of Proposition 1, by a change of variables (and suppressing the variable ω), since $e_j = f(\widetilde{e}_j)$ we deduce

$$\int_{\widetilde{\Omega}} \widetilde{\sigma}(\widetilde{x}) \nabla_{\widetilde{x}} \widetilde{u}_n(\widetilde{x}) \cdot \nabla_{\widetilde{x}} \widetilde{v}(\widetilde{x}) d\widetilde{x} = \int_\Omega (\widetilde{\sigma} \circ F^{-1})(x) (J_F^t \circ F^{-1})(x) \nabla u_n \cdot (J_F^t \circ F^{-1})(x) \nabla v(x) |\det J_{F^{-1}}(x)| \, dx.$$
$$\int_{\widetilde{e}_j} (\widetilde{u}_n - \widetilde{U}_{n,j})(\widetilde{v} - \widetilde{V}_j) d\widetilde{s} = \int_{e_j} (u_n - U_{n,j})(v - V_j) |\det J_{F^{-1}}^S| \, ds,$$

where $v = \widetilde{v} \circ F^{-1} \in H^1(\Omega)$ and $V_j = \widetilde{V}_j$. Hence, the pair $(u_n(\cdot,\omega), U_n(\omega))$ satisfies

$$\int_\Omega \sigma(x,\omega) \nabla u_n(x,\omega) \cdot \nabla v(x) \, dx + \sum_{j=1}^E z_j^{-1} \int_{e_j} (u_n - U_{n,j})(v - V_j) z \, ds = \sum_{j=1}^E I_{n,j} V_j, \qquad (v, V) \in \mathbb{H},$$

where the transformed conductivity $\sigma(x,\omega)$ is given by (3.7). By combining this identity with (4.4), we obtain

$$\int_\Omega (\sigma - \sigma_0) \nabla u_n \cdot \nabla v_m \, dx = \sum_{j=1}^E (I_{n,j} V_{m,j} - I_{m,j} U_{n,j}) + \sum_{j=1}^E \int_{e_j} (z-1)(u_n - U_{n,j}) \frac{\partial v_m}{\partial \nu_{\sigma_0}} \, ds.$$

In view of [25, 26] we can expand z as

$$z = 1 + \varepsilon(\mathrm{Div}\phi_t - (d-1)H\phi_\nu) + O(\varepsilon^2), \quad (4.7)$$

where Div denotes the surface divergence, ϕ_t and ϕ_ν denote the tangential and normal components of the vectorial function ϕ on the boundary $\partial\Omega$, respectively, and H is the mean curvature of $\partial\Omega$. In particular, $z - 1 = O(\varepsilon)$. Therefore, by linearization we can write

$$\int_{e_j} (z-1)(u_n - U_{n,j}) \frac{\partial v_m}{\partial \nu_{\sigma_0}} \, ds \approx \int_{e_j} (z-1)(v_n - V_{n,j}) \frac{\partial v_m}{\partial \nu_{\sigma_0}} \, ds = -z_j \int_{e_j} (z-1) \left(\frac{\partial v_m}{\partial \nu_{\sigma_0}} \right)^2 ds.$$

Inserting this approximation in the above identity we obtain

$$\int_\Omega (\sigma - \sigma_0) \nabla u_n \cdot \nabla v_m \, dx = \sum_{j=1}^E (I_{n,j} V_{m,j} - I_{m,j} U_{n,j}) - \sum_{j=1}^E z_j \int_{e_j} (z-1) \left(\frac{\partial v_m}{\partial \nu_{\sigma_0}} \right)^2 ds.$$

The rest of the proof follows as in Proposition 1, and thus it is omitted. □

By proceeding as in the continuum model, we can rewrite (4.6) as

$$s_0(\omega)\int_\Omega(\varepsilon\Psi+\delta\sigma_0)\nabla v_n^*\cdot\nabla v_m^*\,dx+\sum_{k=1}^K s_k(\omega)\int_\Omega\delta\sigma_k\nabla v_n^*\cdot\nabla v_m^*\,dx$$
$$=s_0(\omega)^2\sum_{j=1}^E(I_{n,j}V_{m,j}-I_{m,j}U_{n,j})-s_0(\omega)\sum_{j=1}^E c_j\int_{e_j}(z-1)\left(\frac{\partial v_m^*}{\partial\nu}\right)^2 ds. \quad (4.8)$$

When compared with the linearized model in the continuum case, cf. (3.11), we observe the presence of the additional error term $s_0(\omega)C_m$, where

$$C_m:=-\sum_{j=1}^E c_j\int_{e_j}(z-1)\left(\frac{\partial v_m^*}{\partial\nu}\right)^2 ds,$$

that comes from the boundary deformation. The formula (4.8) is perfectly consistent with (3.11): in the continuum case, the contact impedance effect is not taken into account, and $u_n=U_n$ on the electrodes, namely $c_j=0$, whence $C_m=0$.

All the preceding analysis easily carries forward to the case $c_j>0$, as we now discuss. Before treating the general case, let us consider the simple scenario where $z\equiv 1$ on the electrodes $\cup_j e_j$.

Example 5. Recall that $z(x)=|\det J_{F^{-1}}^S(x)|$ for x on the boundary $\partial\Omega$. Physically, the factor z represents the length/area deformation relative to the map $F^{-1}\colon\partial\Omega\to\partial\widetilde{\Omega}$, as we remarked earlier. Thus, it may be reasonable to assume that the parametrization of the electrodes $\{e_j\}_{j=1}^E$ is known, which implies $z\equiv 1$ on the electrodes $\cup_j e_j$.

In such a case, we immediately obtain $C_m\equiv 0$, whence

$$s_0(\omega)\int_\Omega(\varepsilon\Psi+\delta\sigma_0)\nabla v_n^*\cdot\nabla v_m^*\,dx+\sum_{k=1}^K s_k(\omega)\int_\Omega\delta\sigma_k\nabla v_n^*\cdot\nabla v_m^*\,dx=s_0(\omega)^2\sum_{j=1}^E(I_{n,j}V_{m,j}-I_{m,j}U_{n,j}).$$

This identity is completely analogous to (3.11), and the same comments on the reconstruction procedure are valid here, since the right hand side is known. In particular, by applying any of the techniques discussed in Section 2 to multifrequency measurements, it is possible to eliminate the error coming from the domain perturbation $\varepsilon\Psi$, as this affects only the inclusion $\delta\sigma_0$ (corresponding to s_0). All the other inclusions $\delta\sigma_k$, $k=1,\dots,K$, may be successfully reconstructed.

Now we consider the general case when $z\not\equiv 1$ on the electrodes $\cup_j e_j$. This corresponds to a situation where the length (or the area) of the electrodes is not precisely known. Thus, the additional error term $s_0(\omega)C_m$ in the linearized model (4.8) has to be taken into account. The key observation is that C_m is independent of the frequency ω. The difference imaging method discussed in Section 2.2 may be directly applied here, provided that $0\notin\mathcal{P}$, i.e., if the frequency profile $s_0(\omega)$ does not vary substantially with respect to the frequency ω. Indeed, in this case the error term $s_0(\omega)C_m$ disappears upon differentiating the relation (4.8), and the inversion step may be performed as in Section 2.2.

The method of Section 2.1 (and, thus, the particular case discussed in Section 2.3) may also be directly applied, since the dependence of the error term $s_0(\omega)C_m$ with respect to the frequency ω follows exactly the spectral profile $s_0(\omega)$. Namely, its influence on the reconstruction step can be essentially lumped into the component $\delta\sigma_0$, like the conductivity perturbation $\varepsilon\Psi$ discussed earlier. Thus, all the inclusions $\delta\sigma_k$, $k=1,\dots,K$, corresponding to the remaining frequency profiles $s_1,\dots,s_K$ may be completely reconstructed. Alternatively, one may see this from the linear system as follows. When multiplying the right hand side of the system of equations associated to (4.8) by S^{-1}, the error term $s_0(\omega)C_m$ cancels

out in all the systems $MA_k = Y_k$, for $k = 1, \ldots, K$. This follows by elementary linear algebra, since

$$[s_0(\omega_1)C\,,\,\ldots\,,\,s_0(\omega_Q)C]\,S^{-1} = C\,[s_0(\omega_1)\,,\,\ldots\,,\,s_0(\omega_Q)]\begin{bmatrix} s_0(\omega_1) & \cdots & s_0(\omega_Q) \\ \vdots & \vdots & \vdots \\ s_K(\omega_1) & \cdots & s_K(\omega_Q) \end{bmatrix}^{-1}$$
$$= [C\,,\,0\,,\,\ldots\,,\,0],$$

where C denotes the column vector corresponding to the error terms C_m (see Example 1 for the simple case when $Q = 2$ and $K = 1$).

5 Group Sparse Reconstruction Algorithm

For all the scenarios discussed in the previous sections, one arrives at a number of (decoupled) linear systems

$$MA_k = Y_k \quad k = 0, \ldots, K, \tag{5.1}$$

where $M \in \mathbb{R}^{J\times L}$ is the sensitivity matrix, $A_k \in \mathbb{R}^L$ are the unknown abundances, and $Y_k \in \mathbb{R}^J$ is a known piece of data. These linear systems are often under-determined, and severely ill-conditioned, due to the inherent ill-posed nature of the EIT inverse problem. Below we describe one strategy for the stable and accurate solution of the linear system (5.1) based on the idea of regularization; we refer to [43, 45, 31] for general discussions on regularization methods.

There are several natural aspects to take into consideration for the regularization term, especially sparsity, grouping, disjoint sparsity and bound constraints.

(1) For $k = 0, 1, 2, \ldots, K$, we can assume that the abundances $A_k = (\delta\sigma_k)_l \in \mathbb{R}^L$ are sparse with respect to the pixel basis (piecewise constant approximation). This suggests minimizing

$$\min_{A_k\in\Lambda} \|A_k\|_1 \quad \text{subject to } \|MA_k - Y_k\| \le \varepsilon_k$$

for each $k = 0, 1, \ldots, K$. Here $\|\cdot\|_1$ denotes the ℓ^1 norm of a vector. The set Λ represents a box constraint on the unknown vector A_k, since the conductivity σ remains bounded from below and above by positive constants, due to physical constraint, and $\varepsilon_k > 0$ is an estimate of the noise level in the data Y_k. This ℓ^1 optimization problem can be solved efficiently by many algorithms, e.g., iterative soft thresholding.

(2) In EIT applications, it is also reasonable to assume that each abundance A_k is clustered, and this refers to the concept of group sparsity. The grouping effect is useful to remove the undesirable spikes typically observed for the ℓ^1 penalty alone. There are several different approaches to this task. The elastic net [33] is one simple way to realize grouping. In this work, we shall develop an approach that is easy to implement, inspired by the dynamic group sparsity proposed in [29]. It allows to dynamically realize group sparsity without knowing the supports of the A_ks nor their sizes.

(3) The support of the inclusions A_k are assumed to be disjoint from each other. The disjoint supports of A_ks can be simply promoted, e.g. by adding a term that penalizes the scalar product of the absolute values of the A_ks [52].

Remark 2. Note that (1) and (2) refer to methods in which the abundances A_ks are recovered separately, while (3) to methods in which all the A_ks are reconstructed simultaneously.

Next we construct an efficient iterative algorithm, termed as group iterative soft thresholding, for achieving the goals outlined above. It combines the strengths of the classical iterative soft thresholding algorithm [14] and the grouping effect in the dynamical group sparse recovery [29]: the former is easy to

implement and has a built-in regularizing effect, whereas the latter encourages the group sparsity pattern. In the implementation, it is a simple modification of the classical iterative soft thresholding algorithm for ℓ^1 optimization (by omitting the subscript k in the abundance): given an initial guess A^0, construct an approximation iteratively by

$$A^{j+1} = S_{s^j\alpha}(g^j),$$

where the proxy g^j is defined by

$$g^j = A^j - s^j M^t(MA^j - Y). \tag{5.2}$$

Observe that $M^t(MA^j - Y)$ is the gradient of the fitting term $\frac{1}{2}\|MA - Y\|^2$ at the current iterate A^j, and hence g^j is essentially a gradient descent update of the current reconstruction A^j. The scalar $\alpha > 0$ is a regularization parameter and $s^j > 0$ is the step length. One simple choice of the step size s^j is the constant one $s^j = 1/\|M\|^2$, which ensures the convergence of the algorithm [14]. The soft thresholding operator S_λ for $\lambda > 0$ is defined by

$$S_\lambda(t) = \max(|t| - \lambda, 0)\,\mathrm{sign}(t),$$

and it is applied componentwise when the argument is a vector.

In the proposed group iterative soft thresholding algorithm, instead of performing the thresholding on the proxy g^j directly, we take into account the neighboring influence. Following [29], this is easily achieved by computing a generalized proxy d_l^j of the lth element by

$$d_l^j = |g_l^j|^2 + \sum_{k\in\mathcal{N}_l} w_{lk}|g_k^j|^2, \tag{5.3}$$

where w_{lk} are nonnegative weights, and $\mathcal{N}_l$ denotes the neighborhood of the lth element. The weights w_{lk} determine the strength of correlation between the components: the smaller the magnitude of w_{lk} is, the weaker the correlation strength between the lth and the kth components is, and if $w_{lk} = 0$ for all $k \in \mathcal{N}_l$, it does not encourage grouping at all. In our implementation, we take $w_{lk} = \beta$, for some constant $\beta > 0$, for all neighboring elements, with a default value $\beta = 0.5$. Physically, in EIT, the neighborhood $\mathcal{N}_l$ of the lth element consists of all elements in the triangulation that share one edge with the lth element, and may be expanded to include also the elements that share one node. Then the vector d^j is used to reweigh the thresholding step by

$$\bar{d}^j = \max(d^j)^{-1} d^j, \tag{5.4}$$

The quantity $\bar{d}^j$ indicates a normalized grouping effect: the larger $\bar{d}_l^j$ is, the more likely the lth element belongs to the group, and thus the less thresholding should be applied to it. This can be easily achieved by rescaling the regularization parameter α to be inversely proportional to $\bar{d}_l^j$, with

$$\bar{\alpha}_l^j = \alpha/\bar{d}_l^j, \quad l = 1, \ldots, L, \tag{5.5}$$

and last perform the projected thresholding with a spatially variable regularization parameter $\bar{\alpha}^j$

$$A^{j+1} = P_\Lambda(S_{s^j\bar{\alpha}^j}(g^j)). \tag{5.6}$$

where P_Λ denotes the pointwise projection onto the constraint set Λ. The complete procedure is listed in Algorithm 1. Here N is the maximum number of iterations. Since the solution A is expected to be sparse, a natural choice of the initial guess A^0 is the zero vector. The regularization parameter α plays a crucial role in the performance of the reconstruction quality: the larger the value α is, the sparser the reconstructed abundance is. There are several strategies available for the classical iterative soft thresholding, e.g., discrepancy principle and balancing principle. In this work, we shall test the feasibility of the algorithm only with the regularization parameter α determined in a trial-and-error manner. One can terminate the algorithm by monitoring the relative change of the iterates.

Algorithm 1 Group iterative soft thresholding.

1: Input M, Y, W, $\mathcal{N}$, α, N and A^0.
2: **for** $j = 1, \ldots, N$ **do**
3: Compute the proxy g^j by (5.2).
4: Compute the generalized proxy d^j by (5.3).
5: Compute the normalized proxy $\bar{d}^j$ by (5.4).
6: Adapt the regularization parameter $\bar{\alpha}^j$ by (5.5).
7: Update the abundance A^{j+1} by the group thresholding (5.6).
8: Check the stopping criterion.
9: **end for**

Last, we note that the disjoint sparsity can be enforced conveniently in Algorithm 1. Specifically, we first compute the normalized proxy $\bar{d}^{k,j}$ for the abundance A_k separately according to (5.4), and then at each component $l = 1, \ldots, L$, we update them by

$$\bar{d}_l^{k,j} = \begin{cases} \bar{d}_l^{k,j} & \text{if } k = k_l^*, \\ \varepsilon & \text{otherwise,} \end{cases} \qquad k_l^* = \underset{k=0,\ldots,K}{\arg\max}\, \bar{d}_l^{k,j},$$

where $\varepsilon > 0$ is a small number to avoid numerical overflow. This step effectively only retains the most likely abundance component (with the likelihood for the kth abundance given by $\bar{d}^{k,j}$), and sets to zero all the remaining ones. Hence, it enforces the disjoint sparsity as desired.

6 Numerical Experiments and Discussions

In this section we present some numerical results to illustrate the analytic study of this work. We treat only the complete electrode model (4.1), since the results for the simpler continuum model (2.1) are similar. The general setting for the numerical experiments below is as follows. The computational domain is taken to be the unit circle $\Omega = \{(x_1, x_2) : x_1^2 + x_2^2 < 1\}$. There are sixteen electrodes $\{e_j\}_{j=1}^E$ (with $E = 16$) evenly distributed along the boundary $\partial\Omega$, each of length $\pi/16$, thus occupying one half of the boundary $\partial\Omega$; see Fig. 1a for a schematic illustration of the electrode placement. The contact impedances $\{z_j\}_{j=1}^E$ on the electrodes $\{e_j\}_{j=1}^E$ are all set to unit, and the background conductivity σ_0 is taken to be $\sigma_0 \equiv 1$. Further, we shall always assume that the spectral profile $s_0(\omega)$ for the background is the constant one $s_0 \equiv 1$. This is not a restriction, since $s_0(\omega)$ is always known, and one can rescale the spectral profiles so that $s_0 \equiv 1$. We measure the electrode voltages U for all 15 sinusoidal input currents. The complete electrode model (4.1) is discretized using a piecewise linear finite element method on a shape regular quasi-uniform triangulation of the domain Ω [20]. The conductivity is represented on a coarser finite element mesh using a piecewise constant finite element basis. The electrode voltages are generated on a much finer mesh in order to avoid the inverse crime. Then the noisy data U^δ is generated by adding componentwise Gaussian noise to the exact data $U^\dagger := U(\sigma^\dagger)$ corresponding to the true conductivity $\sigma^\dagger(x, \omega)$ as follows

$$U_j^\delta = U_j^\dagger + \varepsilon \max_l |U_l^\dagger - U_l(\sigma_0)| \varepsilon_j, \quad j = 1, \ldots, E,$$

where ε is the noise level, and ε_j follows the standard normal distribution.

We shall present the numerical results for the cases of a known boundary and of an imperfectly known boundary separately, and discuss only cases a) and b) with spectral profiles that are either fully known or have substantially different frequency dependence. Case c), corresponding to the case of partially known spectral profiles, will not be discussed, since the inversion is totally analogous to that of case a), except for simple algebraic manipulations. For the solutions of the underdetermined linear systems (5.1), we use the group iterative soft thresholding algorithm listed in Algorithm 1 with a constant step size.

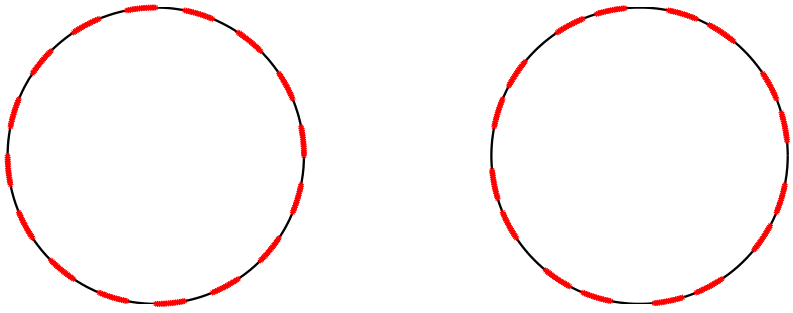

(a) computational domain Ω (b) imperfectly known domain $\widetilde{\Omega}$

Figure 1: The electrode arrangement for the computational domain Ω and for an imperfectly known domain $\widetilde{\Omega}$ (used in Example 9). The curved segments in red denote the electrodes. The electrodes in (a) are equally spaced, but those in (b) are not.

The regularization parameter α used in each separate reconstruction was determined by a trial-and-error manner, and it was set to 10^{-2} for all examples presented below. We did not implement the disjoint sparsity, since in all the examples under consideration the reconstruction are already very satisfactory. However, it is expected that with higher noise levels or in the case of almost touching inclusions, enforcing disjoint sparsity might give enhanced reconstructions. The algorithm is always initialized with a zero vector. Numerically, we observe that it converges steadily and fast. All the computations were performed using MATLAB 2013a on a 2.5G Hz and 6G RAM personal laptop.

6.1 Perfectly Known Boundary

First, we illustrate the approach in the case of a perfectly known boundary.

Example 6. Consider three square inclusions: the two inclusions on the top share the same spectral profile $s_1(\omega)$, and the one on the bottom has a second spectral profile $s_2(\omega)$; cf. Fig. 2a for an illustration. In the experiments, we consider the following two cases:

(i) The spectral profiles $s_1(\omega)$ and $s_2(\omega)$ are given by $s_1(\omega) = 0.1\omega + 0.1$ and $s_2(\omega) = 0.2\omega$.

(ii) The spectral profiles $s_1(\omega)$ and $s_2(\omega)$ are given by $s_1(\omega) = 0.1\omega + 0.1$ and $s_2(\omega) = 0.02\omega$.

In either case, we take measurements at $Q = 3$ frequencies, $\omega_1 = 0$, $\omega_2 = 0.5$ and $\omega_3 = 1$.

The numerical results for Example 6 with $\varepsilon = 1\%$ noise in the data are shown in Figs. 2 and 4 for cases (i) and (ii), respectively. In case (i), the two frequencies have about the same magnitude, and the (rectangular) spectral matrix S is nonsingular. Assuming the knowledge of the spectral profiles, the direct approach discussed in Section 2.1 separates the two sets of inclusions well thanks to their incoherent spectral profiles. The recovery is very localized within a clean background, the supports match closely the true supports (and are clearly disjoint from each other) and the magnitude of the inclusions are well retrieved. The latter observation is a distinct feature of the proposed group sparse recovery algorithm discussed in Section 5. Hence, if both profiles are known exactly and are incoherent, then the two sets of inclusions can be fairly recovered. Case (ii) is similar, except that the variation of the spectral profile $s_2(\omega)$ is now much smaller. The preceding observations remain largely valid, except that the inclusion corresponding to $s_2(\omega)$ involves minor spurious oscillations. This is attributed to the presence of noise in the data: the noise level is comparable with effective contributions from the inclusion. Hence, for the accurate recovery of the inclusions separately, the data should be reasonably accurate, as expected.

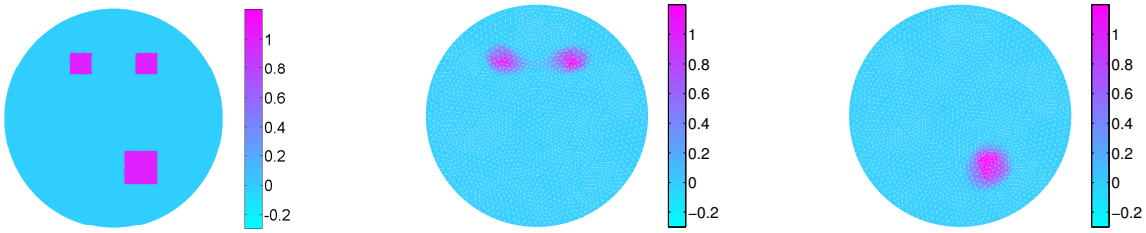

(a) true $\delta\sigma_k$s (b) recovered $\delta\sigma_1$ (c) recovered $\delta\sigma_2$

Figure 2: Numerical results for Example 6(i) with 1% noise in the data, and fully known spectral profiles. The reconstructions were obtained using the direct approach in Section 2.1.

The well-conditioning of the spectral profile matrix S implies the robustness of the direct approach with respect to perturbations of the spectral profiles, as mentioned in Section 2.1. To confirm this, we present in Fig. 3 the reconstructions using imprecisely known spectral profiles, where the spectral matrix is perturbed by additive Gaussian noise with a zero mean and standard deviation proportional to the entry magnitude. Even only with three modulating frequencies, the reconstructions remain fairly stable, up to 20% perturbation of the spectral profiles, indicating the robustness of the approach. This is consistent with the experimental findings in [41], where the feasibility of the abundance separation with imprecise spectral profiles was numerically demonstrated.

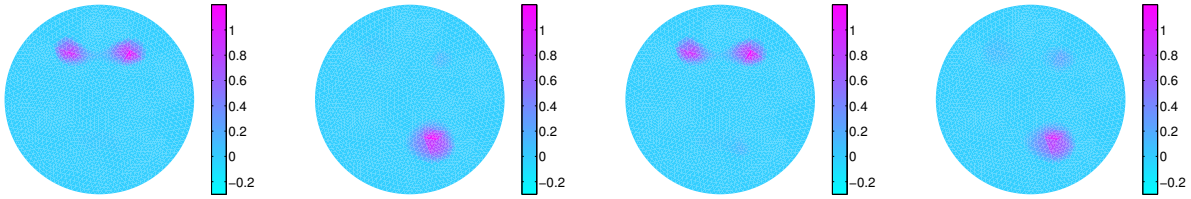

(a) recovered $\delta\sigma_1$ (b) recovered $\delta\sigma_2$ (c) recovered $\delta\sigma_1$ (d) recovered $\delta\sigma_2$

Figure 3: Numerical results for Example 6(i) with 1% noise in the data, and imprecisely known spectral profiles. The reconstructions in (a) and (b) are obtained with the spectral matrix S perturbed by additive Gaussian noise with mean zero and standard deviation 10% of the entry magnitude, and those in (c) and (d) with 20% noise, both by the direct approach in Section 2.1.

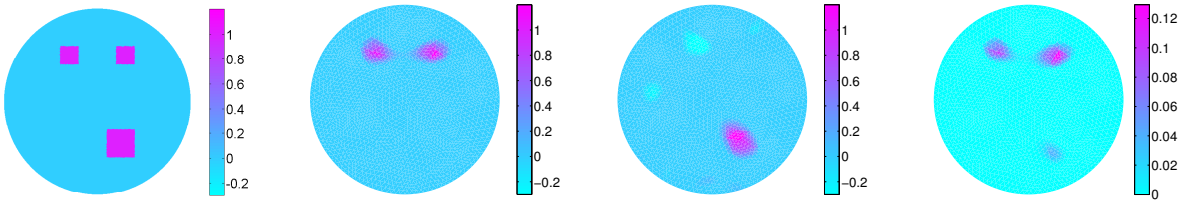

(a) true $\delta\sigma_k$s (b) recovered $\delta\sigma_1$ (c) recovered $\delta\sigma_2$ (d) recovered $\delta\sigma_1$

Figure 4: Numerical results for Example 6(ii) with 1% noise in the data. The reconstructions in panels (b) and (c) are obtained with fully known spectral profiles using the direct approach in Section 2.1, and that in panel (d) is obtained without knowing the spectral profiles, using difference imaging (Section 2.2).

With Example 6(ii), we also illustrate the difference imaging method discussed in Section 2.2.1, which is applicable since the variation of the frequency profile $s_2(\omega)$ is small. The reconstruction of the first set of inclusions, in the absence of the knowledge of the spectral profiles, is shown in Fig. 4d. The reconstruction recovers the inclusions up to a multiplicative constant very well, and it is almost completely free from spurious oscillations. This clearly shows the capability of difference imaging for spectral profiles with substantially different frequency dependence.

Example 7. Consider three rectangular inclusions on the top left, top right and bottom of the disk with spectral profiles $s_1(\omega)$, $s_2(\omega)$ and $s_3(\omega)$, respectively, cf. Fig. 5a for an illustration. In the experiments, we consider the following two cases:

(i) The spectral profiles $s_1(\omega)$, $s_2(\omega)$ and $s_3(\omega)$ are given by $s_1(\omega) = 0.2\omega + 0.2$, $s_2(\omega) = 0.1\omega^2$, and $s_3(\omega) = 0.2\omega + 0.1$, respectively.

(ii) The spectral profiles $s_1(\omega)$, $s_2(\omega)$ and $s_3(\omega)$ are given by $s_1(\omega) = 0.02\omega + 0.02$ and $s_2(\omega) = 0.1\omega^2$, and $s_3(\omega) = 0.2\omega + 0.1$, respectively.

In either case, we take measurements at three frequencies, $\omega_1 = 0$, $\omega_2 = 0.5$ and $\omega_3 = 1$.

The numerical results for Example 7(i) and 7(ii) are shown in Figs. 5 and 6, respectively. If all three spectral profiles are known, the use of three frequencies yields almost perfect separation of the three inclusions by using the method of Section 2.1: the recovered inclusions are well clustered in a clean background, and their supports and magnitudes are correctly identified. Note that in the case of Example 7(ii), the spectral profile $s_1(\omega)$ is much smaller, and thus the recovery of the inclusion $\delta\sigma_1$ is more susceptible to noise, whereas the recovery of the remaining two are far more stable.

The results in Fig. 6 indicate that with known spectral profiles $s_2(\omega)$ and $s_3(\omega)$ and unknown $s_1(\omega)$, since $s_1(\omega)$ varies little with respect to ω, the difference imaging technique proposed in Section 2.2.2 can recover accurately both the magnitude and support of the inclusions $\delta\sigma_2$ and $\delta\sigma_3$. These observations fully confirm the discussions in Section 2.2.

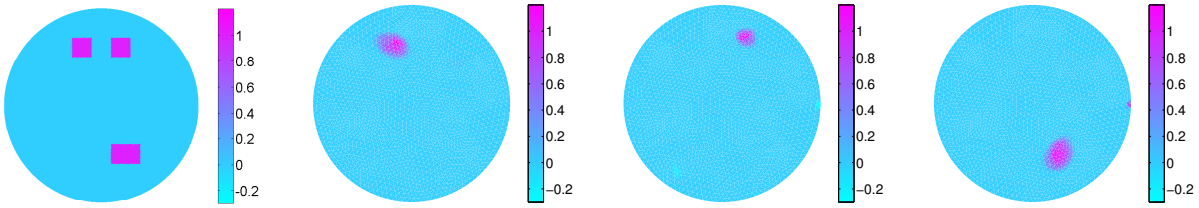

(a) true $\delta\sigma_k$s (b) recovered $\delta\sigma_1$ (c) recovered $\delta\sigma_2$ (d) recovered $\delta\sigma_3$

Figure 5: Numerical results for Example 7(i) with 1% noise in the data, with fully known spectral profiles. The reconstructions are obtained by the direct approach in Section 2.1.

6.2 Imperfectly Known Boundary

Now we illustrate the approach in the case of an imperfectly known boundary. In the first example, the unknown true domain $\widetilde{\Omega}$ is an ellipse centered at the origin with semi-axes a and b, $\mathcal{E}_{a,b} = \{(x_1, x_2) : x_1^2/a^2 + x_2^2/b^2 < 1\}$, and the computational domain Ω is taken to be the unit circle.

Example 8. Consider two square inclusions, on the top and on the bottom of the ellipse, with spectral profiles $s_1(\omega) = 0.2\omega + 0.2$ and $s_2(\omega) = 0.1\omega^2$, respectively (Fig. 7). We consider the following two cases:

(i) The true domain $\widetilde{\Omega}$ is $\mathcal{E}_{a,b}$ with $a = 1.1$ and $b = 0.9$;

(ii) The true domain $\widetilde{\Omega}$ is $\mathcal{E}_{a,b}$ with $a = 1.2$ and $b = 0.8$.

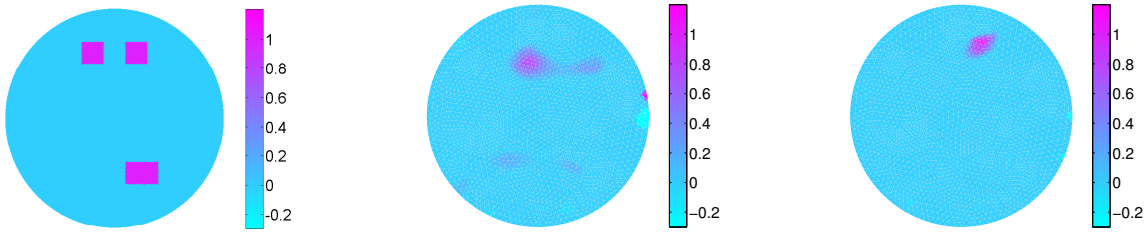

(a) true $\delta\sigma_k$s (b) recovered $\delta\sigma_1$ (c) recovered $\delta\sigma_2$

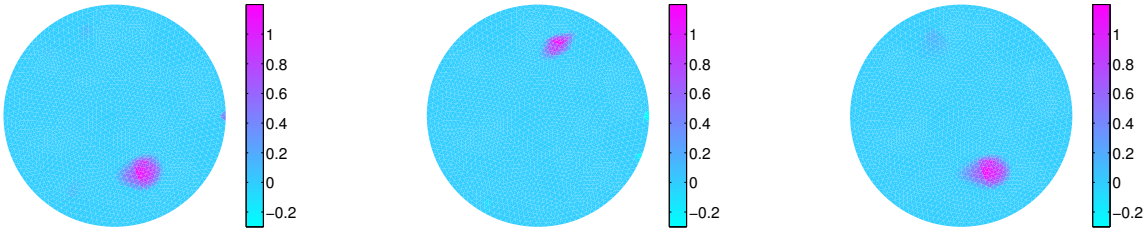

(d) recovered $\delta\sigma_3$ (e) recovered $\delta\sigma_2$ (f) recovered $\delta\sigma_3$

Figure 6: Numerical results for Example 7(ii) with 1% noise in the data. Here (b)-(d) are the reconstructions with fully known spectral profiles, while for (e) and (f) only the spectral profiles $s_2(\omega)$ and $s_3(\omega)$ are known, and the reconstructions are obtained by difference imaging (Section 2.2).

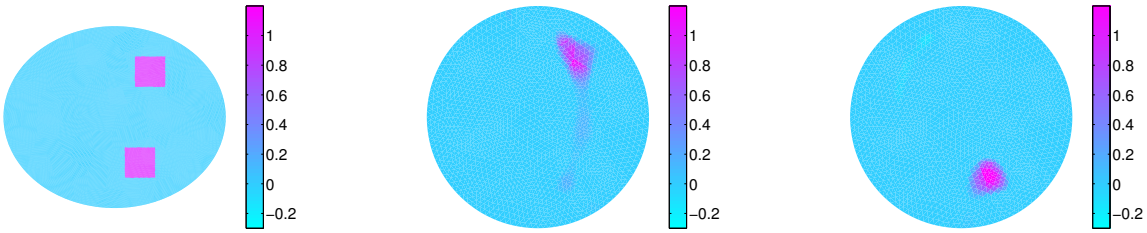

(a) true $\delta\sigma_k$s (b) recovered $\delta\sigma_1$ (c) recovered $\delta\sigma_2$

Figure 7: Numerical results for Example 8(i) with 0.1% noise in the data, fully known spectral profiles. The reconstructions are obtained using difference imaging in Section 2.2.

In either case, we take three frequencies, $\omega_1 = 0$, $\omega_2 = 0.5$ and $\omega_3 = 1$.

The numerical results are given in Figs. 7 and 8 with 0.1% noise in the data, for cases (i) and (ii), respectively. Even though not presented, we note that a direct application of the classical EIT imaging technique can only produce useless reconstruction, due to the presence of significant modelling errors. Numerically one can verify that for both cases, the contribution from domain deformation is actually one order of magnitude larger than that due to the genuine inclusions, which justify the smaller noise level 0.1%. By exploiting the frequency incoherence, the multi-frequency EIT allows the separation of the contributions from different abundances, and hence recovering each inclusion accurately.

From Fig. 7, we observe that the difference imaging from Section 2.2.2 can recover the two inclusions accurately, and further, the two inclusions can be well separated, due to their incoherent spectral profiles. However, the shape of the recovered inclusion tends to be slightly deformed and location slightly shifted.

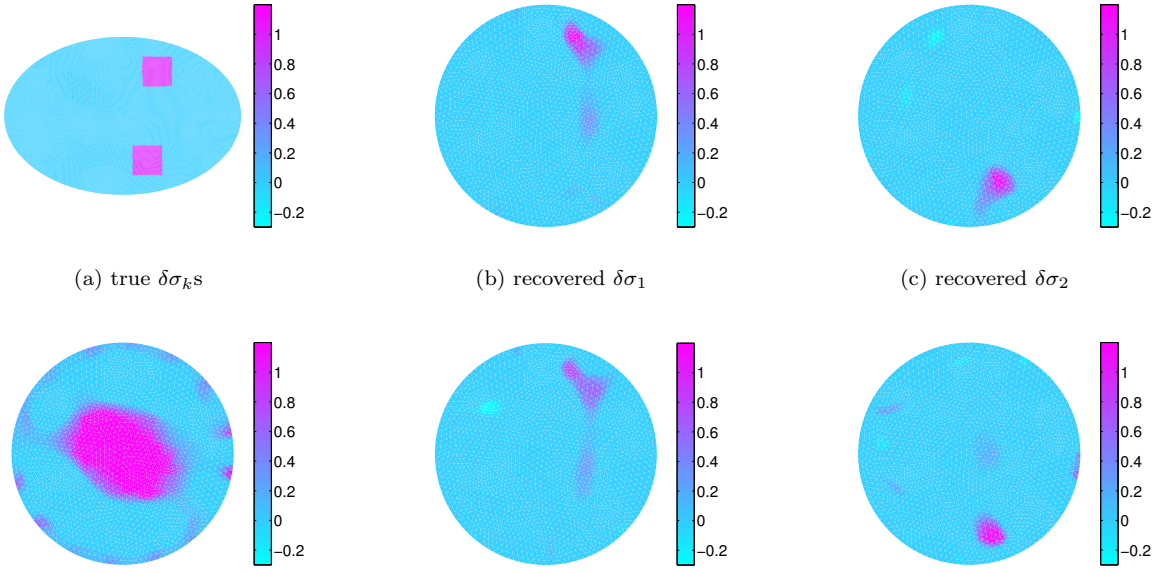

(a) true $\delta\sigma_k$s (b) recovered $\delta\sigma_1$ (c) recovered $\delta\sigma_2$

(d) recovered $\delta\sigma_0$ (e) recovered $\delta\sigma_1$ (f) recovered $\delta\sigma_2$

Figure 8: Numerical results for Example 8(ii) with 0.1% noise in the data, fully known spectral profiles. The reconstructions in panels (b)-(c) are based on difference imaging technique of Section 2.2, and those in panels (d)-(f) are based on the direct approach in Section 2.1.

This is consistent with the discussions in Section 4: the unknown boundary induces a slightly deformed conductivity of the inclusions, in addition to the anisotropic component.

In Fig. 8 we present the results related to Example 8(ii). The preceding observations on difference imaging still hold, cf. Fig. 8a and 8b. The direct approach of Section 2.1 works equally well: the recovered $\delta\sigma_1$ and $\delta\sigma_2$ are fairly accurate in terms of the location and magnitude; and the results are comparable with those obtained by difference imaging. Surely, the recovered $\delta\sigma_0$ contains only the spurious conductivity induced by the domain deformation. Should there be any true inclusion $\delta\sigma_0$ corresponding to the spectral profile $s_0(\omega)$, it will be completely washed away by the deformation error $\varepsilon\Psi$ in (4.8). The preceding discussions fully confirm the analysis in Section 4: the multifrequency approach is capable of discriminating the perturbation due to domain deformation from the genuine inclusions by either the direct approach in Section 2.1 or the difference imaging discussed in Section 2.2.

Last we present one example where the electrodes are misplaced, but the length of the electrodes do not change, i.e., the factor z in the boundary integral can be set to the unit (see Example 5). This is a special case of the imperfectly known boundary case, where the forward map F maps the domain Ω onto itself. However, the forward map is not the identity or a rotation operator, and thus it will induce an anisotropic conductivity, especially in the regions near the boundary.

Example 9. The true domain $\widetilde{\Omega}$ is identical with the computational domain Ω, the unit circle, but every other electrode is shifted by an angle of $\pi/32$, while the length of each electrode remains unchanged; see Fig. 1(b) for a schematic illustration. There are two rectangular inclusions, on the top and on the bottom of the ellipse, with spectral profiles $s_1(\omega) = 0.2\omega + 0.2$ and $s_2(\omega) = 0.1\omega^2$, respectively. We take the measurement at three frequencies $\omega_1 = 0$, $\omega_2 = 0.5$ and $\omega_3 = 1$.

The numerical results for Example 9 are summarized in Fig. 9. The analysis in Section 3 and in Section 4.2 indicates that the conductivity perturbation due to the domain deformation can be limited to the background component $\delta\sigma_0$, as above. The numerical results confirm the analysis: when using the

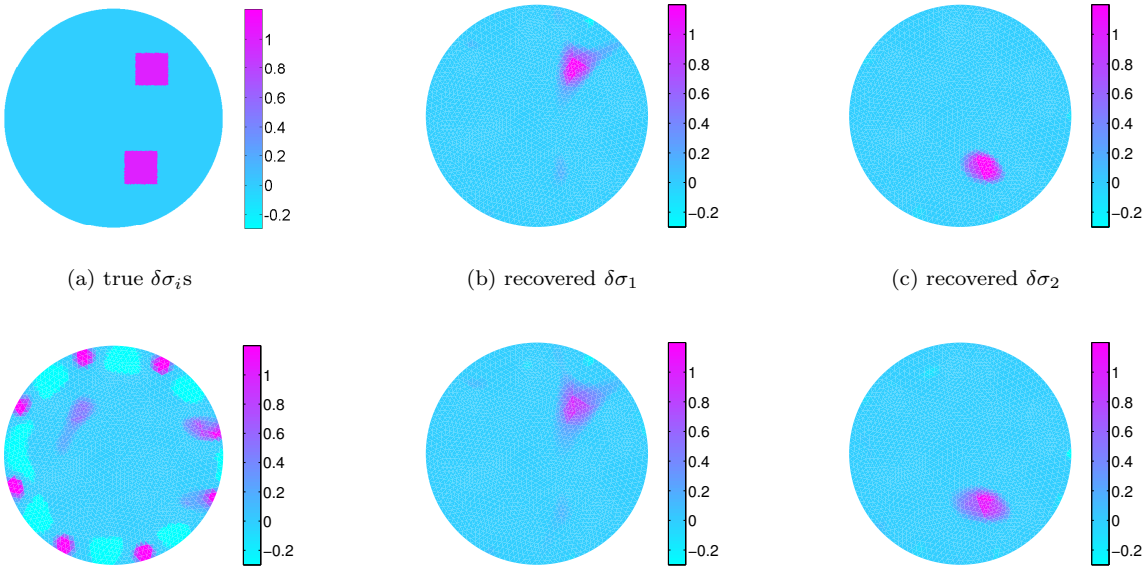

(a) true $\delta\sigma_i$s (b) recovered $\delta\sigma_1$ (c) recovered $\delta\sigma_2$

(d) recovered $\delta\sigma_0$ (e) recovered $\delta\sigma_1$ (f) recovered $\delta\sigma_2$

Figure 9: Numerical results for Example 9 with 0.1% noise in the data, fully known spectral profiles. The reconstructions shown in panels (b)-(c) are based on difference imaging in Section 2.2, whereas those in panels (d)–(f) are based on the direct approach in Section 2.1.

direct approach discussed in Section 2.1, there are many pronounced perturbations around the boundary in the reconstructed $\delta\sigma_0$, due to the domain deformation. However, the reconstructed $\delta\sigma_1$ and $\delta\sigma_2$ are fairly reasonable in terms of location and size, albeit slightly deformed. The difference imaging can also remove the contributions due to unknown electrode locations and separate the contributions from the two inclusions. This is feasible since the frequency profiles are incoherent both before and after the differentiation.

In summary, as expected from the analysis of Sections 3 and 4.2, the mfEIT technique has significant potentials in handling modelling errors. The inclusion $\delta\sigma_0$ corresponding to the background frequency profile s_0 may not be reconstructed. However, by using the multifrequency approach, the remaining inclusions $\{\delta\sigma_k\}_{k=1}^K$ can be correctly recovered by either the direct approach in Section 2.1 or the difference imaging in Section 2.2, provided that the corresponding spectral profiles (or their derivatives) are sufficiently incoherent.

7 Concluding remarks

In this paper we have presented novel reconstruction methods in multifrequency EIT. In particular, we have illustrated both analytically and numerically the potential of mfEIT in handling the modelling error due to an imperfectly known boundary shape. We have also introduced a new and efficient group sparse reconstruction algorithm for the linearized EIT problem. It is expected that the techniques introduced in this paper can be extended to quantitative photoacoustic imaging from spectral measurements [51].

Acknowledgements

This work was partially supported by the ERC Advanced Grant Project MULTIMOD-267184 and the EPSRC grant EP/M025160/1.

References

[1] A. Adler, R. Gaburro, and W. Lionheart. Electrical impedance tomography. In O. Scherzer, editor, *Handbook of Mathematical Methods in Imaging*, pages 599–654. Springer New York, 2011.

[2] A. Adler, R. Guardo, and Y. Berthiaume. Impedance imaging of lung ventilation: do we need to account for chest expansion? *IEEE Trans. Biomed. Eng.*, 43(4):414–420, 1996.

[3] H. Ammari. *An introduction to mathematics of emerging biomedical imaging.* Springer-Verlag, Berlin, 2008.

[4] H. Ammari, E. Bonnetier, Y. Capdeboscq, M. Tanter, and M. Fink. Electrical impedance tomography by elastic deformation. *SIAM J. Appl. Math.*, 68(6):1557–1573, 2008.

[5] H. Ammari, S. Boulmier, and P. Millien. A mathematical and numerical framework for magnetoacoustic tomography with magnetic induction. *J. Differential Equations*, 259(10):5379–5405, 2015.

[6] H. Ammari, J. Garnier, L. Giovangigli, W. Jin, and J.-K. Seo. Spectroscopic imaging of a dilute cell suspension. *J. Math. Pures Appl.*, page doi:10.1016/j.matpur.2015.11.009, 2016.

[7] H. Ammari, P. Grasland-Mongrain, Millien, L. Seppecher, and J.-K. Seo. A mathematical and numerical framework for ultrasonically-induced Lorentz force electrical impedance tomography. *J. Math. Pures Appl.*, 103(6):1390–1409, 2015.

[8] H. Ammari and H. Kang. *Reconstruction of small inhomogeneities from boundary measurements.* Springer-Verlag, Berlin, 2004.

[9] H. Ammari, O. Kwon, J.-K. Seo, and E.-J. Woo. T-scan electrical impedance imaging system for anomaly detection. *SIAM J. Appl. Math.*, 65(1):252–266, 2004.

[10] H. Ammari, E. Lee, H. Kwon, J.-K. Seo, and E.-J. Woo. Mathematical modeling of mechanical vibration-assisted conductivity imaging. *SIAM J. Appl. Math.*, 75(3):1031–1046, 2015.

[11] H. Ammari and J. Seo. An accurate formula for the reconstruction of conductivity inhomogeneities. *Adv. in Appl. Math.*, 30(4):679–705, 2003.

[12] L. Borcea. Electrical impedance tomography. *Inverse Problems*, 18(6):R99R136, 2002.

[13] K.-S. Cheng, D. Isaacson, J. C. Newell, and D. G. Gisser. Electrode models for electric current computed tomography. *IEEE Trans. Biomed. Eng.*, 36(9):918–924, 1989.

[14] I. Daubechies, M. Defrise, and C. De Mol. An iterative thresholding algorithm for linear inverse problems with a sparsity constraint. *Comm. Pure Appl. Math.*, 57(11):1413–1457, 2004.

[15] P. J. Davis. *Interpolation and approximation.* Blaisdell Publishing Co. Ginn and Co. New York-Toronto-London, 1963.

[16] C. Gabriel, A. Peyman, and E. H. Grant. Electrical conductivity of tissue at frequencies below 1MHz. *Phys. Med. Biol.*, 54(16):4863–4878, 2009.

[17] S. Gabriely, R. W. Lau, and C. Gabriel. The dielectric properties of biological tissues: II. Measurements in the frequency range 10 Hz to 20 GHz. *Phys. Med. Biol.*, 41(11):2251–2269, 1996.

[18] B. Gebauer and O. Scherzer. Impedance-acoustic tomography. *SIAM J. Appl. Math.*, 69(2):565–576, 2008.

[19] L. A. Geddes and L. E. Baker. The specific resistance of biological material – a compendium of data for the biomedical engineeer and physiologist. *Med. & Biol. Engng*, (3):271–293, 1967.

[20] M. Gehre, B. Jin, and X. Lu. An analysis of finite element approximation in electrical impedance tomography. *Inverse Problems*, 30(4):045013, 24, 2014.

[21] E. Gersing, B. Hofmann, and M. Osypka. Influence of changing peripheral geometry on electrical impedance tomography measurements. *Med. Biol. Eng. Comput.*, 34(5):359–361, 1996.

[22] J. F. Grcar. Spectral condition numbers of orthogonal projections and full rank linear least squares residuals. *SIAM J. Matrix Anal. Appl.*, 31(5):2934–2949, 2010.

[23] H. Griffiths and A. Ahmed. A dual-frequency applied potential tomography technique: computer simulations. *Clin. Phys. Physiol. Meas.*, 8(4A):103–107, 1987.

[24] M. Hanke and O. Scherzer. Inverse problems light: numerical differentiation. *The Amer. Math. Monthly*, 108(6):512–521, 2001.

[25] F. Hettlich. Fréchet derivatives in inverse obstacle scattering. *Inverse Problems*, 11(2):371–382, 1995.

[26] F. Hettlich. Erratum: Frechet derivatives in inverse scattering. *Inverse Problems*, 14(1):209–210, 1998.

[27] D. Holder. *Electrical Impedance Tomography: Methods, History and Applications*. Institute of Physics, Bristol, 2005.

[28] R. Holm. *Electric Contacts: Theory and Applications*. Springer-Verlag, Berlin Heidelberg, 1967.

[29] J. Huang, X. Huang, and D. Metaxas. Learning with dynamic group sparsity. In *2009 IEEE 12th Int. Conf. Computer Vision*, pages 64–71, 2009.

[30] J.-H. Hwang, K. Kirkpatrick, T. Mason, and E. Garboczi. Experimental limitations in impedance spectroscopy: Part iv. electrode contact effects. *Solid State Ionics*, 98(12):93–104, 1997.

[31] K. Ito and B. Jin. *Inverse Problems: Tikhonov Theory and Algorithms*. World Scientific Publishing Co. Pte. Ltd., Hackensack, NJ, 2015.

[32] J. Jang and J. K. Seo. Detection of admittivity anomaly on high-contrast heterogeneous backgrounds using frequency difference EIT. *Phys. Meas.*, 36(6):1179–1192, 2015.

[33] B. Jin, D. A. Lorenz, and S. Schiffler. Elastic-net regularization: error estimates and active set methods. *Inverse Problems*, 25(11):115022, 26, 2009.

[34] N. Keshava and J. F. Mustard. Spectral unmixing. *IEEE Signal Proc. Mag.*, 19(1):44–57, 2002.

[35] S. Kim and A. Tamasan. Reconstructing small perturbations in electrical admittivity at low frequencies. *Inverse Problems*, 30(3):035006, 18, 2014.

[36] V. Kolehmainen, M. Lassas, and P. Ola. The inverse conductivity problem with an imperfectly known boundary. *SIAM J. Appl. Math.*, 66(2):365–383, 2005.

[37] V. Kolehmainen, M. Lassas, and P. Ola. Electrical impedance tomography problem with inaccurately known boundary and contact impedances. *IEEE Trans. Med. Imag.*, 27(10):1404–1414, 2008.

[38] O. Kwon, J.-K. Seo, and J.-R. Yoon. A real-time algorithm for the location search of discontinuous conductivities with one measurement. *Comm. Pure Appl. Math.*, 55(1):1–29, 2002.

[39] S. Laufer, A. Ivorra, V. E. Reuter, B. Rubinsky, and S. B. Solomon. Electrical impedance characterization of normal and cancerous human hepatic tissue. *Physiol. Meas.*, 31(7):995–1009, 2010.

[40] E. Malone, G. Sato dos Santos, D. Holder, and S. Arridge. Multifrequency electrical impedance tomography using spectral constraints. *IEEE Trans. Med. Imag.*, 33(2):340–350, 2014.

[41] E. Malone, G. Sato dos Santos, D. Holder, and S. Arridge. A reconstruction-classification method for multifrequency electrical impedance tomography. *IEEE Trans. Med. Imag.*, 34(7):1486–1497, 2015.

[42] L. Qiu and F. Santosa. Analysis of the magnetoacoustic tomography with magnetic induction. *SIAM J. Imaging Sci.*, 8(3):2070–2086, 2015.

[43] O. Scherzer, M. Grasmair, H. Grossauer, M. Haltmeier, and F. Lenzen. *Variational Methods in Imaging*. Springer, New York, 2009.

[44] J. Schlappa, E. Annese, and H. Griffiths. Systematic errors in multi-frequency EIT. *Physiol. Meas.*, 21(1):111–118, 2000.

[45] T. Schuster, B. Kaltenbacher, B. Hofmann, and K. S. Kazimierski. *Regularization Methods in Banach Spaces*. Walter de Gruyter GmbH & Co. KG, Berlin, 2012.

[46] J. K. Seo, J. Lee, S. W. Kim, H. Zribi, and E. J. Woo. Frequency-difference electrical impedance tomography (fdEIT): algorithm development and feasibility study. *Phys. Meas.*, 29(8):929–944, 2008.

[47] J.-K. Seo and E.-J. Woo. Magnetic resonance electrical impedance tomography (MREIT). *SIAM Rev.*, 53(1):40–68, 2011.

[48] E. Somersalo, M. Cheney, and D. Isaacson. Existence and uniqueness for electrode models for electric current computed tomography. *SIAM J. Appl. Math.*, 52(4):1023–1040, 1992.

[49] A. Surowiec, S. Stuchly, J. Barr, and A. Swarup. Dielectric properties of breast carcinoma and the surrounding tissues. *Biomedical Engineering, IEEE Transactions on*, 35(4):257–263, April 1988.

[50] J. Sylvester. An anisotropic inverse boundary value problem. *Comm. Pure Appl. Math.*, 43(2):201–232, 1990.

[51] A. Taruttis and V. Ntziachristos. Advances in real-time multispectral optoacoustic imaging and its applications. *Nature Photonics*, 9:219–227, 2015.

[52] K. Vervier, P. Mahé, D'Aspremont, J.-B. Veyrieras, and J.-P. Vert. On learning matrices with orthogonal columns or disjoint supports. In *LNCS 8726*, pages 274–289. Springer-Verlag, 2014.

[53] T. Widlak and O. Scherzer. Hybrid tomography for conductivity imaging. *Inverse Problems*, 28(8):084008, 28 pp., 2012.

[54] R. J. Yerworth, R. H. Bayford, B. Brown, P. Milnes, M. Conway, and D. S. Holder. Electrical impedance tomography spectroscopy (EITS) for human head imaging. *Physiol. Meas.*, 24(2):477–489, 2003.